









RESEARCH ARTICLE | JUNE 23 2023

BAMline—A real-life sample materials research beamline

Ana Guilherme Buzanich ; Martin Radtke ; Kirill V. Yusenko ; Tomasz M. Stawski ; Anicó Kulow ; Cafer Tufan Cakir ; Bettina Röder ; Christoph Naese ; Ralf Britzke; Michael Sintschuk; Franziska Emmerling 



J. Chem. Phys. 158, 244202 (2023)

<https://doi.org/10.1063/5.0157194>



View
Online



Export
Citation

CrossMark

Articles You May Be Interested In

Fully automated, fixed exit, in vacuum double-multilayer monochromator for synchrotron-based hard X-ray micro-imaging applications

AIP Conference Proceedings (June 2010)

Dimensional Control of Micro Components with Synchrotron Computed Tomography

AIP Conference Proceedings (April 2010)

Quantitative studies on inner interfaces in conical metal joints using hard x-ray inline phase contrast radiography

Rev. Sci. Instrum. (October 2010)

500 kHz or 8.5 GHz?
And all the ranges in between.

Lock-in Amplifiers for your periodic signal measurements



Find out more

 Zurich
Instruments

BAMline—A real-life sample materials research beamline

Cite as: J. Chem. Phys. 158, 244202 (2023); doi: 10.1063/5.0157194

Submitted: 5 May 2023 • Accepted: 9 June 2023 •

Published Online: 23 June 2023



View Online



Export Citation



CrossMark

Ana Guilherme Buzanich,^{1,a)} Martin Radtke,¹ Kirill V. Yusenko,¹ Tomasz M. Stawski,¹
Anicó Kulow,^{1,2} Cafer Tufan Cakir,¹ Bettina Röder,¹ Christoph Naese,¹ Ralf Britzke,¹
Michael Sintschuk,¹ and Franziska Emmerling^{1,3}

AFFILIATIONS

¹Federal Institute of Materials Research and Testing (BAM), Richard-Willstaetter-Str. 12, 12489 Berlin, Germany

²Univ. Grenoble Alpes, CNRS, Grenoble INP, Institut Néel, 38000 Grenoble, France

³Department of Chemistry, Humboldt-Universität zu Berlin, Brook-Taylor-Str. 2, 12489 Berlin, Germany

^{a)} Author to whom correspondence should be addressed: ana.buzanich@bam.de

ABSTRACT

With increasing demand and environmental concerns, researchers are exploring new materials that can perform as well or better than traditional materials while reducing environmental impact. The BAMline, a real-life sample materials research beamline, provides unique insights into materials' electronic and chemical structure at different time and length scales. The beamline specializes in x-ray absorption spectroscopy, x-ray fluorescence spectroscopy, and tomography experiments. This enables real-time optimization of material properties and performance for various applications, such as energy transfer, energy storage, catalysis, and corrosion resistance. This paper gives an overview of the analytical methods and sample environments of the BAMline, which cover non-destructive testing experiments in materials science, chemistry, biology, medicine, and cultural heritage. We also present our own synthesis methods, processes, and equipment developed specifically for the BAMline, and we give examples of synthesized materials and their potential applications. Finally, this article discusses the future perspectives of the BAMline and its potential for further advances in sustainable materials research.

© 2023 Author(s). All article content, except where otherwise noted, is licensed under a Creative Commons Attribution (CC BY) license (<http://creativecommons.org/licenses/by/4.0/>). <https://doi.org/10.1063/5.0157194>

I. INTRODUCTION

The world faces major sustainability challenges, such as climate change and the depletion of natural resources, which require innovative solutions. As the population continues to grow and the demand for resources increases, it has become clear that we need to find new, sustainable ways to make materials. In a traditional approach, materials have been intuitively selected based on their specific and tangible performance criteria, such as strength and toughness, durability, or degradation resistance. However, under such general selection paradigms, materials are often derived from non-renewable resources and can have a significant environmental impact during their production, use, and disposal. Therefore, researchers are exploring new materials that can perform as well or better than traditional materials but with a lower environmental impact. To achieve these goals, obtaining multifaceted information about all aspects of the synthesis, functioning, and degradation of materials is crucial. This entails characterizing the multi-length scale

structure of new materials, so one can understand their properties and behavior under different physicochemical conditions as they “function,” i.e., *in situ*, in a time-resolved manner. This kind of state-of-the-art characterization is achieved at multi-purpose beamlines, such as the BAMline. The beamline offers characterization techniques at different time and length scales and specializes in x-ray absorption spectroscopy (XAS), x-ray fluorescence spectroscopy (XRF), and tomography experiments.^{1,2} This suite of techniques can provide unique insights into a wide range of material systems of different levels of complexity. Using the methods available at the BAMline, researchers can study the electronic and chemical structure of materials. The invaluable as-derived information can be applied in areas as diverse as materials synthesis, energy transfer, energy storage, catalysis, corrosion, and degradation studies.

Measurements at the BAMline offer real-time insights into the syntheses of new materials and, therefore, provide the basis to improve their properties and optimize their performance both at a fundamental level, in processes, and devices. For example, in energy

transfer applications, XAS can be used to study dynamically and *in situ* the electronic structure of materials used in solar cells, such as metal chalcogenides, and to optimize their performance. Similarly, XAS routinely delivers insights about the electronic structure of materials used in other energy transfer devices, such as thermoelectrics, and photovoltaics, helping to develop more efficient and sustainable technologies.

This article provides an overview of the analytical methods and sample environments available at the hard x-ray beamline BAMline at BESSY II. The beamline is dedicated to non-destructive testing experiments for research in materials science, chemistry, biology, medicine, and cultural heritage. Many analytical developments document the aim of the BAMline team to meet the analytical requirements in close cooperation with research groups from all over the world. We will also discuss the future perspectives of the BAMline.

II. OVERVIEW OF BAMline

A. General aspects and purpose of the BAMline

The Federal Institute for Materials Research and Testing (BAM) has been operating the experimental station BAMline at the electron storage ring BESSY II (Berlin Electron Storage Ring for Synchrotron Radiation) together with the Helmholtz Center Berlin (HZB) for more than 20 years. The BAMline is the only beamline within BESSY II that covers a spectrum of the hard x-ray range up to 100 keV and is thus an important building block in the overall concept of BESSY II and the Analytical City Adlershof in Berlin. Several institutes, universities, companies, and numerous start-ups are in this one neighborhood.

In recent years, methods such as XAS and XRF have been implemented in different modalities and unique configurations that have become attractive to the community of materials scientists and chemists. The BAMline offers analytical capabilities that are crucial for various applications, such as catalysis and electrocatalysis, which require temporal and spatial resolution, *in situ* formation mechanisms, using time-resolved x-ray spectroscopy, and corrosion mechanisms, which require high spatial resolution in both areal and

depth domains. The new developments have not yet been presented in the context of specific applications in chemistry. An overview of the fields and applications of x-ray spectroscopy at BAMline during the last 10 years is summarized in Fig. 1(a). The analytical needs for z-ray spectroscopy to study different stages of materials research (from synthesis to device) are presented in Fig. 1(b).

B. Technical details of the BAMline

The BAMline was the first hard x-ray beamline established at BESSY II from HZB. It was originally developed and installed by the BAM and the National Metrology Institute of Germany (PTB). The first setup included an insertion device (i.e., a wavelength shifter, WLS), filters, slits, a double crystal monochromator (DCM), and an output window. Beamline operation started in 2001. Three years later, the beamline was extended by a double multilayer monochromator (DMM).³ In 2019, the DMM was replaced by a new three-stripe multilayer optics as the latest upgrade. This upgrade has enhanced the analytical capabilities of the beamline so that a larger spectrum of applications can be covered. The current layout of the BAMline and its optical elements are displayed in Fig. 2.

The radiation source is a superconducting three-pole wavelength shifter (WLS) with a maximum field of 7 T at the central pole and a characteristic energy of 13.5 keV. The WLS was manufactured by the Budker Institute of Nuclear Physics (Novosibirsk, Russia).⁴ The most important parameters of the device are given in Fig. 2, showing the resulting photon flux density at the experiment calculated by REFLEC⁵ for a typical ring current of 300 mA. The specific x-ray energy requirements of a given experiment determine the available photon flux. Thus, depending on the energy, one expects, e.g., different exposure times.

After the latest upgrade in 2019, the beamline has two monochromators: a three-stripe optics that includes two DMM and one mirror and a higher resolution double crystal monochromator (DCM) (Fig. 2). The substrates of the DMM were coated with three 20 mm wide stripes at AXO GmbH (Dresden, Germany). The first one is a metallic mirror of 40 nm palladium. The other two are multilayer structures: one coating W/Si with peak and integral reflectivity,

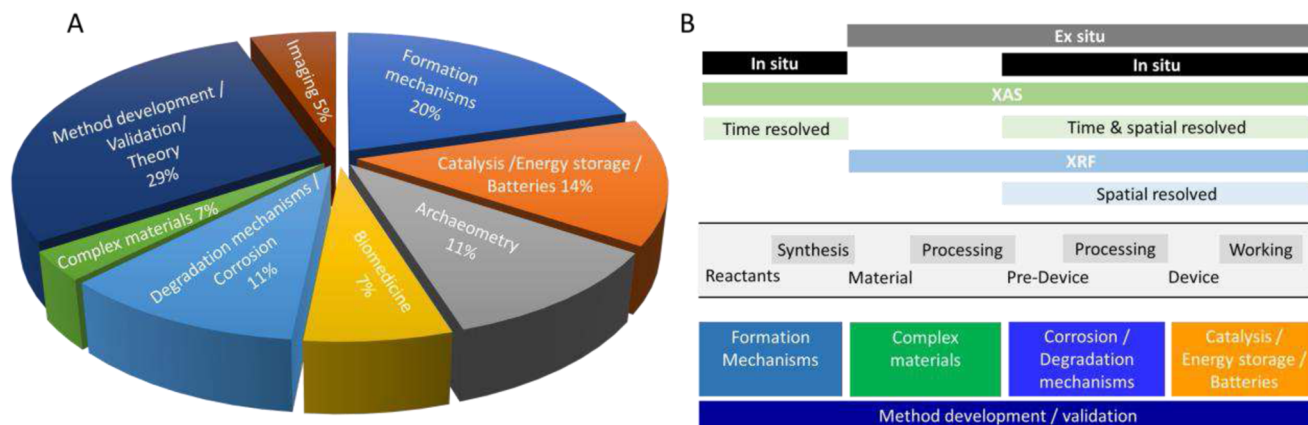


FIG. 1. Overview of the fields of applications using x-ray spectroscopy methods available at the BAMline in the last 10 years (a). Summary of the analytical needs to study different stages of materials research in connection to the applications (b).

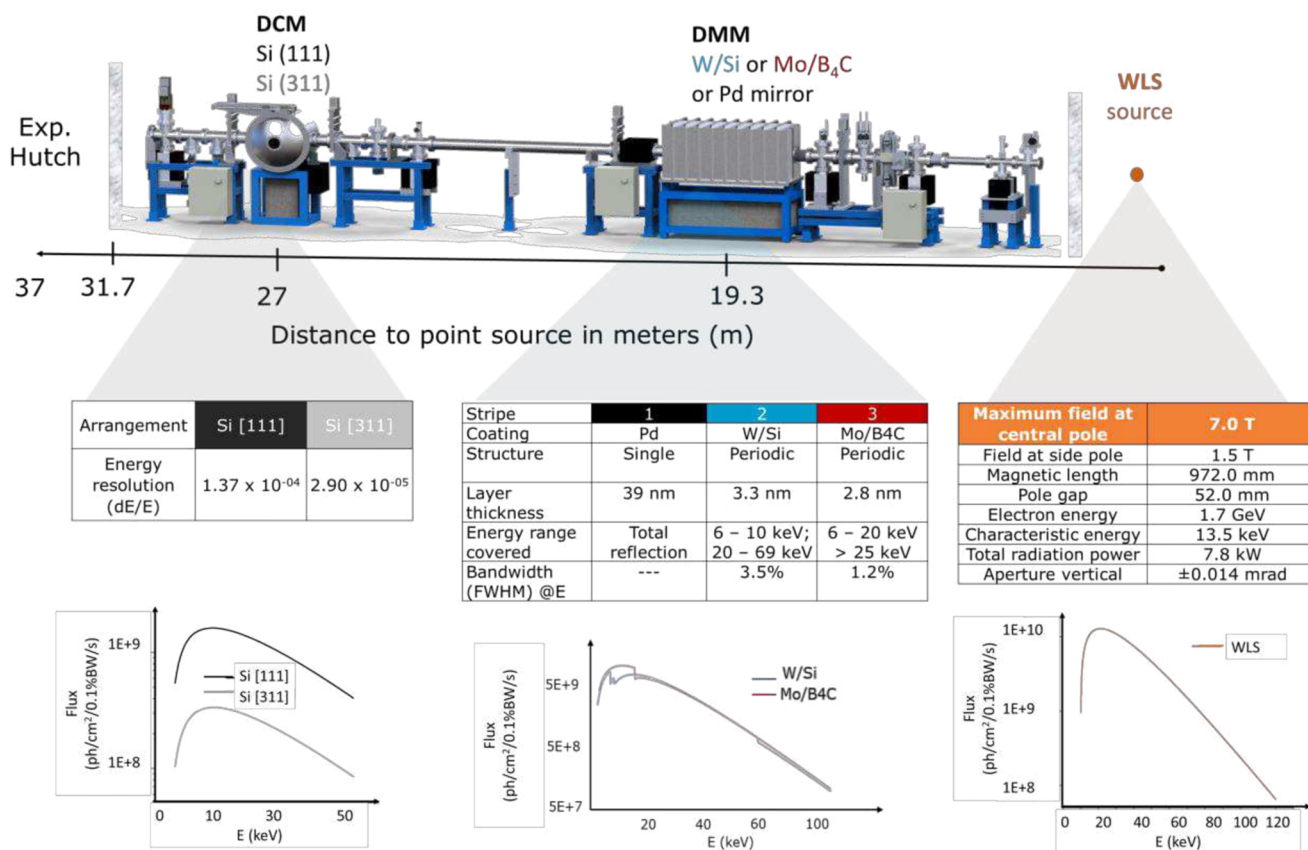


FIG. 2. Layout of the BAMline with its optical elements, summarizing properties, and flux density curves for the whole energy range available.

such as the full width at half maximum (FWHM) in the order of 3%; and the second one Mo/B₄C, which covers the spectrum portion bits suppressed by W/Si. To select one of the stripes, the entire DMM (including the vacuum chamber) is moved perpendicular to the direction of the beam by ± 25 mm.

The DCM from year 2000 was the first type of a monochromator installed at the BAMline. It belongs to the class of monochromators that combine a rotational movement (to select the Bragg angle) for both crystals with two translations for the second crystal. The mechanical heart of the monochromator is a small volume 20:1 planetary gear, which is characterized by coaxial shafts, the transmission of high torques and low imbalance, and a stepper motor with 200 steps. The theoretical half-step motor resolution is 0.45 in., which means for the energy resolution at 10 keV, a minimum value of ΔE of about 0.1 eV for the Si (111) crystal. The DCM can either be equipped with a pair of Si (111) or Si (311) crystals. The resulting flux densities were calculated by REFLEC⁵ (Fig. 2). For standard x-ray absorption spectroscopy measurements, the energy resolution given by the DCM is essential. The energy resolution $\Delta E/E$ of the monochromator is 1.37×10^{-4} for the Si (111) and 2.90×10^{-5} for Si (311).⁵

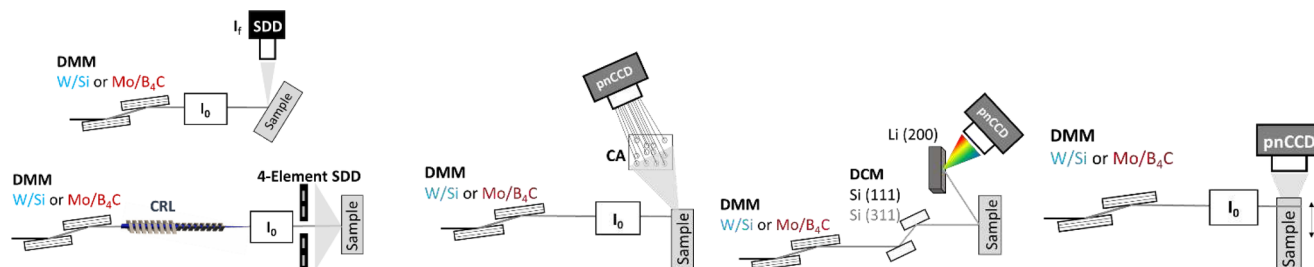
C. Overview of x-ray spectroscopy methods @BAMline

The available analytical methods can be divided into two groups: x-ray spectroscopy and computed tomography (CT).² In the field of spectroscopy, the BAMline provides different modes, such as XRF and XAS. An overview of the x-ray spectroscopy methods available at the BAMline is given in Tables I and II, respectively. Tables I and II summarize the technical details, applications, and sketches of the setups. Actual pertinent fields of investigation are, among others, catalysis, “green chemistry,” energy storage, corrosion, biology, medicine, and environment.^{6–10}

X-ray fluorescence (XRF) is the emission of characteristic x rays from a material that has been excited by high-energy x rays or gamma rays. XRF is a non-destructive analytical technique for determining element concentrations. Depending on the detection method, a distinction is made between wavelength-dispersive and energy-dispersive XRF. Both are available in different geometries at the BAMline. XRF experiments require an excitation energy above the absorption edges of the elements of interest. Generally, the DMM is employed in most XRF configurations due to its higher flux. However, the DCM is used for XAS measurements in XRF

TABLE I. Overview of x-ray fluorescence spectroscopy (XRF) methods available at the BAMline: standard and micro-x-ray fluorescence spectroscopy (XRF), coded aperture-x-ray fluorescence spectroscopy (CA-XRF), double-dispersive x-ray fluorescence spectroscopy (D²XRF), and slicing x-ray fluorescence spectroscopy (Slicing-XRF). DMM: double multilayer monochromator, DCM: double crystal monochromator, SDD: silicon drift detector, and pnCCD: pn-semiconductor junction with the charge-coupled device.

	Standard and Micro-XRF ^{11–17}	Coded aperture XRF (CA-XRF) ^{18,19}	Double dispersive XRF (D ² XRF) ^{20–23}	Mapping (Slicing-XRF) ^{24–26}
Time resolution	Different scan modes such as on the fly, step or Bayesian optimized available. On-the-fly: up to 200 points per second	15 min resolution to obtain a 2D distribution	Photon-hungry experiment. Not suitable for time resolved experiments. One spectrum takes up to 1 h	Sheet-like incident beam; minimum voxel size 10 min per layer
Spatial /energy resolution	Adjustable focus down to 1 μm spot size with compound refractive based lenses (CRL)	Possible to resolve 100 μm . Energy range covered: 4–30 keV	High energy resolution XRF (down to 13 eV) covering a whole 1 keV energy range in one shot. Energy range covered: 4–30 keV	3D information with a spatial resolution of $2 \times 8 \times 8 \mu\text{m}^3$ by vertically sample movement. Energy range covered: 4–30 keV
Sensitivity	2D XRF maps on elements with tens of $\mu\text{g/g}$ possible. Energy range covered: 4–40 keV	Lens-less imaging with multi-pinhole apertures and a 2D energy dispersive detector. A reconstruction procedure is necessary. 30 ng elemental deposition possible to analyze	Best limit of detection (LOD) reported in XRF: 0.9 $\mu\text{g/g}$ of Pt in 99.9% Au	Alternative to computed tomography in XRF mode. No reconstruction procedure needed
Applications	Elemental distribution and quantification of key elements in catalyst materials, biological samples	2D and 3D imaging of key elements in materials for catalytic devices; insight into biological character played by key elements	Investigation of difficult-to-quantify element combinations in alloys such as platinum in gold; promising for determination of low Z atoms using high energy x-ray by detection of secondary scattering effects (x-ray Raman)	Determination of 3D elemental distributions. Works best for the analysis of medium to high Z elements in a light matrix, such as Cd in cacao beans or Fe in teeth

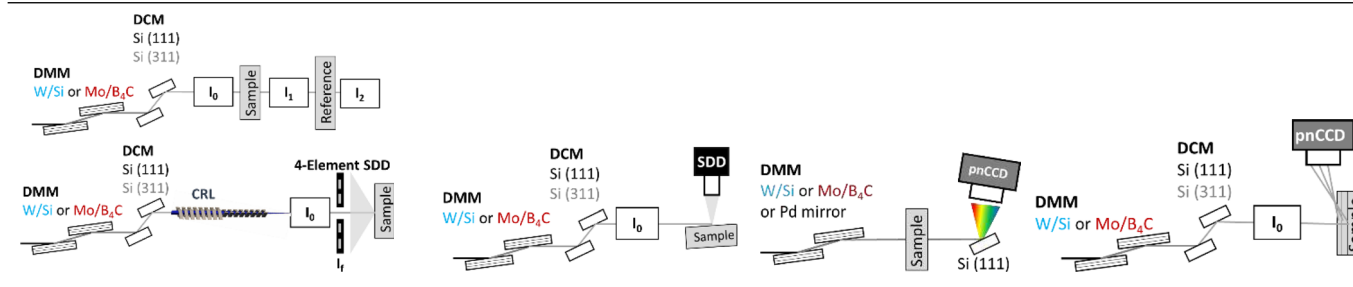


mode or when the resolution of two adjacent absorption edges is required to suppress unwanted signals. The fact that the measurement setup is not in vacuum limits the detection of lighter elements, with the detection capability typically starting at sodium (Na, $Z > 11$). More details are found in Sec. II D. The available XRF modalities are standard and micro-XRF, coded aperture XRF (CA-XRF), double dispersive XRF (D²XRF), and slicing, respectively, x-ray sheet microscopy (XSM).

X-ray absorption spectroscopy (XAS) is an excellent analytical method for probing chemical bonds, the geometry of the crystal structure, and local atomic arrangement (coordination) around the absorbing atom. At the BAMline, XAS can be performed on all elements heavier than calcium (Ca, $Z > 20$). This provides information about the electronic structure, coordination number, interatomic distances, and even thermal disorder around a selected atom. Its element-sensitive character allows inferring the fine structure of the

TABLE II. Overview of x-ray absorption spectroscopy (XAS) methods available at the BAMline: standard and micro-x-ray absorption spectroscopy (XAS), total-reflection x-ray fluorescence-x-ray absorption spectroscopy (TXRF-XAS), dispersive x-ray absorption spectroscopy (DXAS), and grazing-exit x-ray absorption spectroscopy (GE-XAS). DMM: double multilayer monochromator, DCM: double crystal monochromator, SDD: silicon drift detector, and pnCCD: pn-semiconductor junction with the charge-coupled device.

Standard and Micro-XAS ^{6,27,28}	Total reflection XRF-XAS (TXRF-XAS) ^{29,30}	Dispersive XAS (DXAS) ^{10,31,32}	Grazing exit XAS (GE-XAS) ³³	
Time resolution	Step-by-step energy scan with the DCM to obtain the XANES or EXAFS spectrum, with 10 and 20 min time resolution, respectively	Not suitable for time-resolved experiments. Monochromatic incident energy under an angle that fulfills the total reflection. One spectrum can take up to 2 h to collect	This is ideal for time resolved experiments. Whole spectrum in one shot, down to 1 s time resolution	Monochromatic beam can be scanned step by step or Bayesian optimized. In step by step, a whole spectrum can take up to 20 h; in Bayesian optimized, this is improved down to 30 min per spectrum
Spatial /energy resolution	Adjustable focus with CRL lens down to 1 μm spot size. Energy resolution of 0.2 eV	Energy resolution of 0.2 eV	Broad beam: 20 mm (horizontal) \times 8 mm (vertical): Spatial resolved XAS, down to $\sim 10 \mu\text{m}$. Broadband incident energy beam: $E_0 \pm 3.5\%$ for XANES and total reflection from Pd mirror or white beam for EXAFS	Few nanometers (nm) depth resolution. Energy resolution of 0.2 eV
Sensitivity	For standard XAS experiments, powders are diluted with boron nitride or cellulose; solution concentrations are adjusted	Ultra-trace elemental detection (pico- to femtograms); maximum 10 μl of solution deposited on a quartz reflector	Sample homogeneity plays a crucial role here. Shaking sample has proven to overcome most of these hurdles	The element of interest should be the major or minor element to detect. Not suitable for traces in $\mu\text{g/g}$ amounts
Applications	<i>Ex situ</i> characterization of samples in a broad range of applications: catalysis, electrocatalysis, complex compositional alloys, and corrosion phenomena	Redox characterization of key elements used as catalysts, e.g., rhenium-based solutions as alternative to technetium	Follow crystallization processes via mechanochemical routes; characterize catalyst materials at work, where, e.g., gradient reduction or oxidation processes	Investigate corrosion processes in compositionally complex alloys (CCAs); characterization of thin films, e.g., where the growth of crystals is achieved by layer-by-layer deposition of the reactant solutions



absorption profile of photons by a given atom irrespective of the structure, either crystalline or amorphous, in solids, liquids, or even gases. Different modes of operation are available at the BAMline, with different sensitivities to answer analytical questions, depending on the nature of samples. In a classical configuration, XAS

experiments require scanning of a high-resolution monochromatic incident energy around an absorption edge (E_0). This is achieved using the DCM with either Si [111] or Si [311] arrangements, depending on the desired resolution. We developed a dispersive XAS (DXAS) setup that uses a broadband energy incident beam, which

is achieved by using the DMM or the white beam. DXAS enables us to collect a broad energy XAS spectrum in a single shot, without any need for energy scanning, which allows studying fast reactions. Further details are found in Sec. II D.

Moreover, the BAMline provides various XAS modalities: standard and micro-XAS for routine analysis of, e.g., powders and mapping, total reflection XRF-XAS (TXRF-XAS), dispersive XAS (DXAS), and grazing-exit XAS (GE-XAS) for thin film analysis. These specific modalities offer different time, spatial, and energy resolutions to cover a broad range of applications. The specific values, sensitivities, and applications are summarized in Tables I and II. In addition, a schematic of the beamline configuration together with sample positioning aids the fast assignment whether the measurements can be performed in transmission or not.

D. Sample environments and experimental hutch capabilities

Typical questions in materials research range from material synthesis, to understanding and improving materials' properties, and to designing devices based on performance. The studies listed in Sec. III are examples of the kind of information about material synthesis, structure, and performance that can be obtained using x-ray spectroscopy. Measurements at the BAMline place certain demands on the sample shape, which are determined by the method used (Tables I and II) and a required x-ray wavelength range. For example, such requirements may limit a possible maximum sample thickness, concentration, and kinetics. On the other hand, such necessary tinkering with a sample form may potentially affect the representativeness and the physicochemical conditions. Therefore, it is essential to develop and validate a sample environment that matches as realistically as possible the actual sample conditions to

obtain chemical and structural insights over high time and/or spatial resolution. After careful discussion about the question at stake, sometimes users bring their own setups, but often we develop and/or adapt the current sample environments. We have the possibility to 3D print various materials, e.g., PEEK, Teflon, polycarbonate, and PVC, and to develop more complex sample environments, such as cells, where, e.g., high temperature and gas mixture are required to perform *in operando* catalytic studies. A few examples of in house developed sample environments are shown in Fig. 3.

The possibility to accommodate various sample environments results from the design of the BAMline [Fig. 4(a)]. Contrary to other experimental stations at BESSY II, the BAMline is quite spacious, with a volume of $\sim 90 \text{ m}^3$. As a multipurpose beamline, there are four experimental tables that cover different groups of experiments: a table for computed tomography and imaging,² a table for x-ray reflectometry, a table for XRF and XAS experiments (Fig. 4), and a new table only for standard XAS experiments, optimal for extended x-ray absorption fine structure (EXAFS) spectroscopy experiments, with the possibility for automatic gas filling of the ionization chambers (Fig. 4). Thanks to the available gas connections, in conjunction with various sample environments, *in situ* and *in operando* experiments can be carried out. The beamline is equipped with nitrogen (N_2), argon (Ar), and hydrogen (H_2) lines. Other gases can be supplied, e.g., methane (CH_4), helium (He), and oxygen (O_2).

III. SCIENTIFIC CASE STUDIES

The scientific output derived from experiments at the BAMline can be divided in two groups: (A) own method development to improve the beamline capabilities and (B) applications of the developed methods in collaboration with partners from complementary disciplines. Selected examples from these two categories are described in Secs. III A and III B.

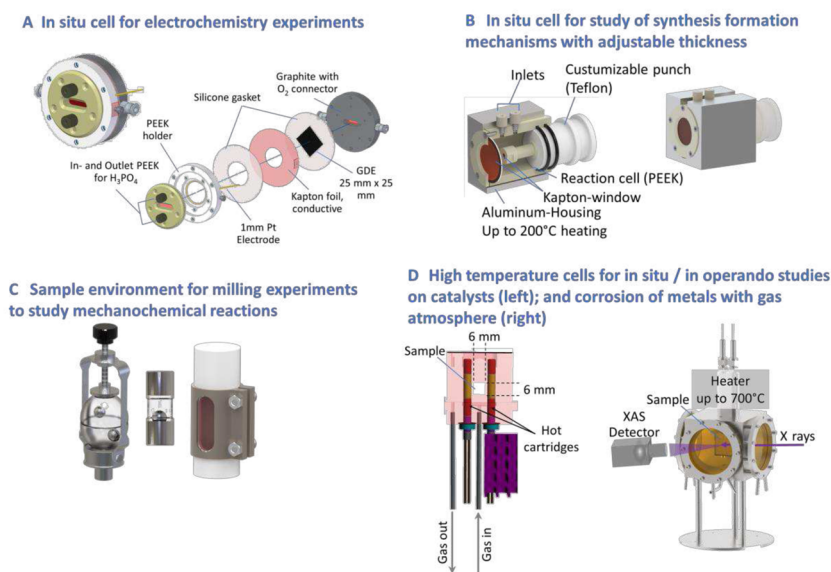


FIG. 3. Examples of sample environments available to perform XRF and XAS experiments at the BAMline under various conditions.^{9,10,34} (Source: own design.)

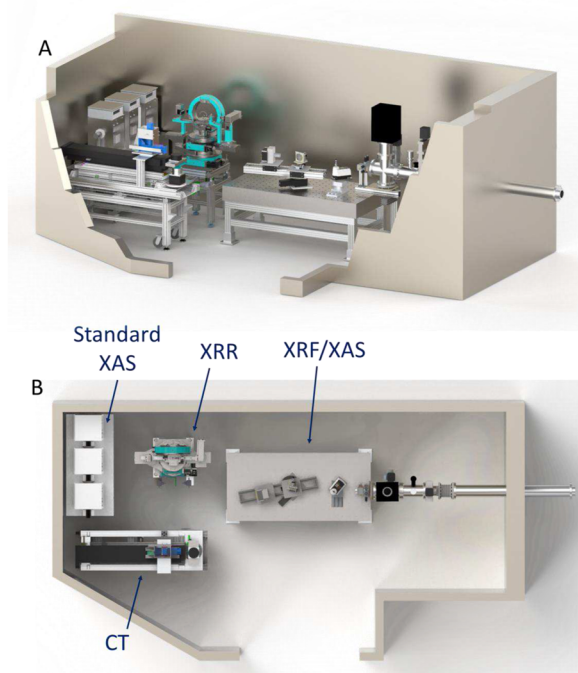


FIG. 4. Overview of the BAMline hutch exterior. Side view (a) and top view with labels for standard XAS, joint XRF/XAS table, and CT and x-ray reflectometry (XRR) (b).

A. Own method development

1. Dispersive x-ray absorption spectroscopy (DXAS)

Investigations of synthesis mechanisms at the BAMline can help to design and optimize materials with improved properties, leading to more efficient and sustainable technologies. Time-resolved XAS experiments are very attractive to follow dynamic processes in real time, offering insight into a material's electronic structure and local coordination environment, as these aspects evolve. However, depending on the configuration and sample, typical XAS measurements rely on mechanical monochromators that can be relatively slow (minutes to hours) to scan the needed energy range for one spectrum, limiting the applicability of the method for time-resolved measurements. We have solved this problem by developing a special setup that belongs to the category of dispersive XAS. A dispersive element is required to produce a polychromatic beam carrying information from the entire XAS range in one exposure. Contrary to other dispersive XAS setups, ours uses the dispersive element after the sample. The incident broadband energy beam is generated either by the W/Si multilayer ($E \pm 3.5\%$) or by the Pd mirror, reflecting a wide range of the spectrum, or by directly using the white beam. Together with an appropriate choice of filters to suppress the unwanted low energy part of the spectrum, this forms an energetic bandpass to define the energy range that interacts with the sample. The transmitted beam is diffracted by a convexly bent Si[111] crystal and, in turn, is collected by a CCD detector. The setup follows a conventional θ - 2θ geometry [Fig. 5(a)]. In this way,

unwanted scattering is suppressed, and the detector is not overexposed by a direct x-ray beam.³² The setup is aligned only once at the beginning of the experiment based on the element to be measured and whether the near edge range (XANES) or the extended part of the spectrum (EXAFS) is required. With this methodology, one can achieve a time resolution of 1 s. Several successful cases are reported.³⁵ Here, we highlight the case study of mechanochemical reactions.

Over the last two decades, mechanochemistry has become a popular, environmentally friendly alternative to solution-based synthesis methods. Neat grinding, liquid-assisted grinding (LAG), and polymer-assisted grinding (POLAG) are highly efficient methods for the preparation of inorganic, organometallic, and organic compounds. Recent reviews and chapters provide more details on these techniques.^{36,37} Mechanochemistry has been identified by the International Union of Pure and Applied Chemistry (IUPAC) as one of the “ten chemical innovations that will change our world”³⁸ due to its exceptional potential for sustainable synthetic strategies. Mechanochemical reactions offer great potential as environmentally friendly methods, but their use is limited by a lack of understanding. *Ex situ* analysis has provided some insight into the mechanisms at play, yet many transformations occur too quickly to be captured this way or are unstable in atmospheric conditions and can change upon extraction from the grinding apparatus. To realize their full potential, time-resolved *in situ* methods must be employed for further exploration.

For the first time, we showed that time resolved *in situ* dispersive XAS is applicable to follow mechanochemical processes in real time. We studied Resonant Acoustic Mixer (RAM)-induced (i) bottom-up Au nanoparticle mechanosynthesis and (ii) the synthesis of a prototypical metal organic framework (MOF), ZIF-8.¹⁰ Moreover, we demonstrated that our approach also worked despite the use of a stainless-steel milling ball, which moved in the beam and could potentially affect the quality of the measured spectrum. In mechanochemistry, the presence of milling media is often considered to be a potential hindrance for *in situ* characterisation,³⁹ yet it is crucial for the effectiveness of the processes. To illustrate, an overview of the results referring to the synthesis of ZIF-8 is displayed in Fig. 5(b). The same reaction was performed twice, with and without including a milling ball, while acquiring XAS data every 2 s at the Zn K-edge (9.569 keV). The starting material ZnO is characterized by a single absorption maximum, while ZIF-8 results in a splitting of the main absorption, giving rise to two maxima. Without the ball, the reaction is completed in 80% after 15 min, while with the ball, it is completed after merely 2 min [Fig. 5(b)]. At the same time, the as-obtained XAS spectra in both scenarios were of a comparable quality. This unprecedented insight into a material's electronic structure is suitable for studying mechanochemical reactions in new reactors (resonant acoustic mixer) and conventional ball mills and is applicable to various material syntheses, including nanoparticle and metal-organic framework mechanosynthesis.¹⁰

2. Grazing-exit x-ray absorption spectroscopy with pnCCD detector (GE-XAS)

The prevention of corrosion damage is a global challenge that requires the development of new materials and a better understanding of corrosion mechanisms. In particular, reactions at pseudo-two-dimensional surface interfaces are critical to the resistance of

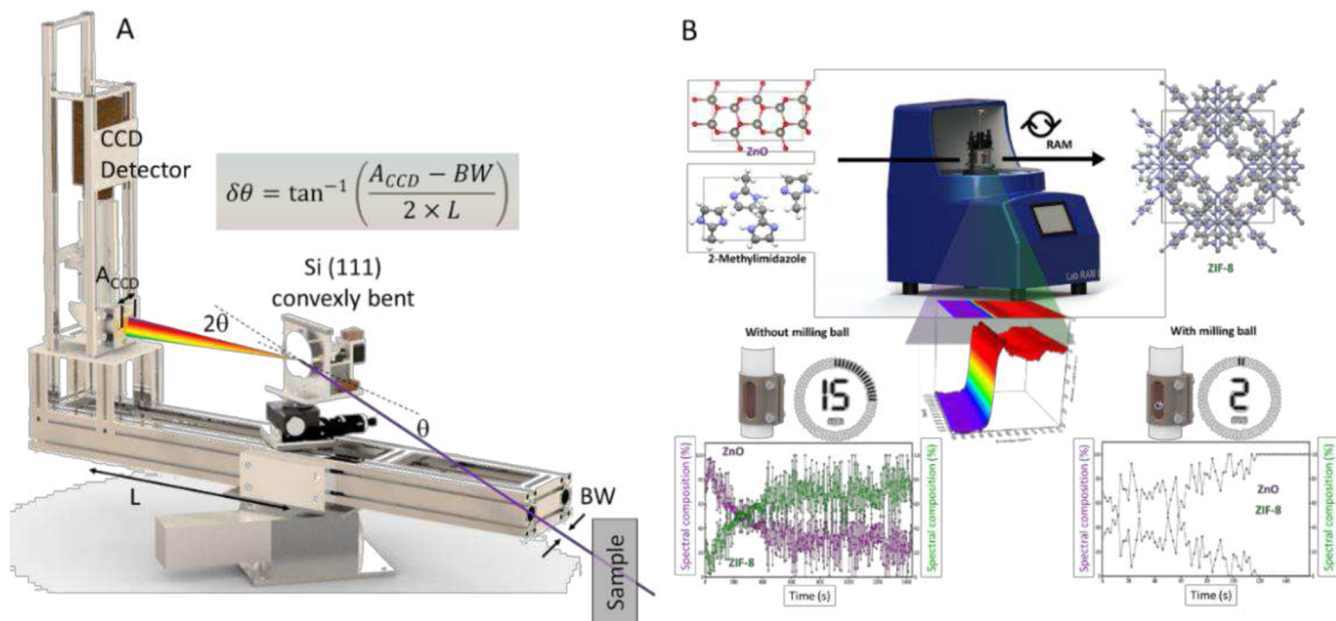


FIG. 5. DXAS setup at the BAMline (a). XAS results obtained for mechanochemical synthesis, ZIF-8 synthesis without and with milling ball (b) [Reproduced and adapted from Guilherme Buzanich *et al.*, “Dispersive x-ray absorption spectroscopy for time-resolved *in situ* monitoring of mechanochemical reactions,” *J. Chem. Phys.* **157**, 214202 (2022) with the permission of AIP Publishing].

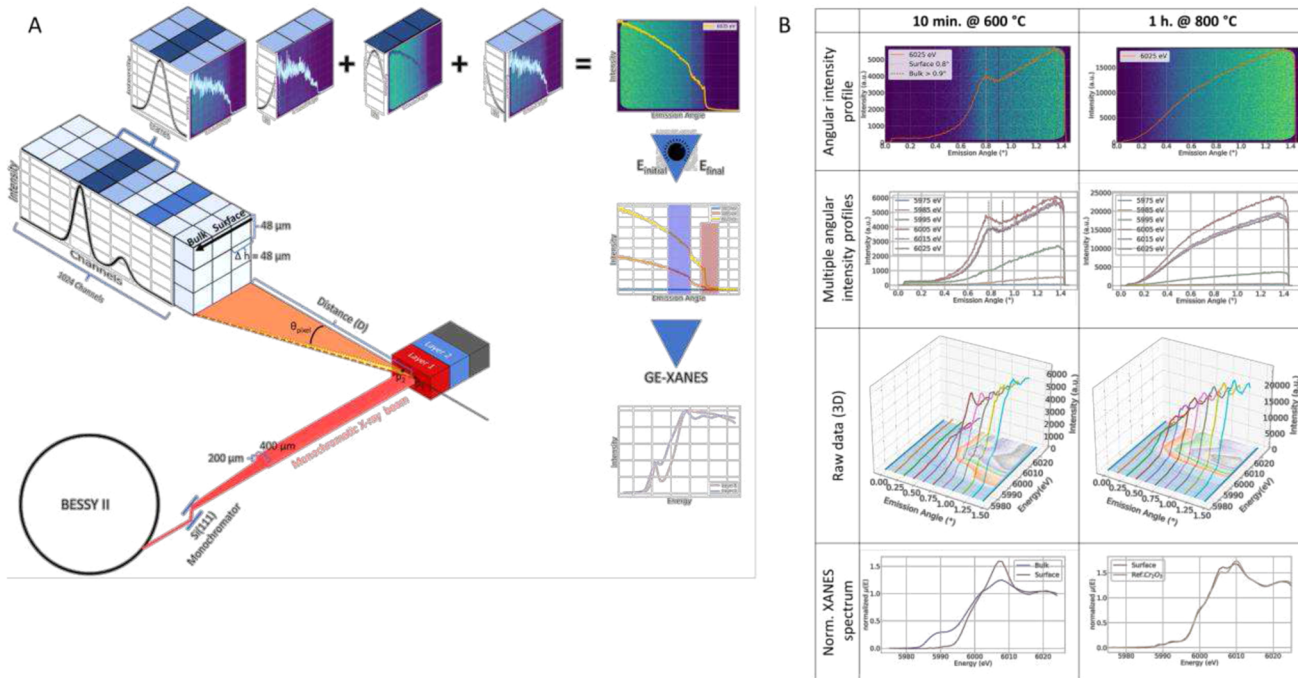


FIG. 6. Working principle of grazing-exit XAS (GE-XAS) setup (a). Depth resolved XAS data at Cr K-edge (5.989 keV) from a CrCoNi alloy after 10 min @ 600 °C and 1 h @ 800 °C [Reproduced with permission from Cakir *et al.*, *Anal. Chem.* **95**, 4810 (2023). Copyright 2023 American Chemical Society].

materials to corrosion. Therefore, the development of surface sensitive non-destructive methods that allow for a direct characterization of electronic properties and structure is crucial. For instance, a new class of materials known as compositionally complex alloys (CCAs) are promising candidates to be used in extreme conditions, such as high temperature or corrosive atmospheres.^{40,41} Simplifying, CCAs contain a plethora (typically >5, but fewer are also possible) of metal elements at close-to-equimolar concentrations: far more than the currently used classical alloys. Classical alloy compositions usually rely on a few, typically two, dominant metal elements and optional “dopants” at lower concentrations. Examples are bronze (composed of copper and tin) and brass (a combination of copper and zinc). In this regard, the corrosion of the classical alloys is assumed to be driven by the processes occurring to the majority metal component(s). CCAs offer superior properties for industrial use compared to traditional alloys, but their corrosion mechanisms remain largely unknown due to the presence of multiple equivalent metal atoms. We developed a method combining depth and energy sensitive information for non-destructive, element specific XAS characterization. Our approach uses the well-established principle of detecting angular intensity profiles at a specific XRF line with grazing exit angles (GE-XRF).^{42,43} In addition, we use a pnCCD detector consisting of ~70 000 pixels, each comparable to a silicon drift detector (SDD) with a size of $48 \times 48 \mu\text{m}^2$ measuring a full XRF spectrum.⁴⁴ This allows us to directly identify and fit the x-ray line of interest, minimizing any overlapping artifacts, such as scattering or other unwanted x-ray lines. The measurements require a monochromatic incident x-ray beam that is finely scanned around the desired absorption edge. The beam size is kept at $400 \times 200 \mu\text{m}^2$, a compromise between higher count rate and lower topological effects. The beam irradiates the sample under 90° , and the detector is placed to measure the fluorescence signal under small angles with respect to the sample surface beam. After this, x-ray fluorescence is emitted and detected under a grazing exit angle. The covered solid angle is determined by the sample-to-detector distance (D) [Fig. 6(a)].³³

CrCoNi medium entropy CCA alloy samples were tempered in air either 600°C for 10 min or to 800°C for 1 h. GE-XAS measurements were performed at the Cr K-edge (5.989 keV) on both samples. The sequence for obtaining the depth-resolved XAS data is the following: (1) we select a Cr-K α fluorescence line, (2) we plot the intensity of this line vs an exit angle (angular intensity profile), (3) we construct a 3D plot of all angular intensity profiles for each incident x-ray energy around the Cr K-edge (XAS data), and (4) we plot and compare the different as-normalized XAS data. The results of these steps (1–4) are displayed in Fig. 6(b). At 600°C for 10 min, there is a clear difference in Cr oxidation state (CrO_3 on top of Cr-metal); at 800°C for 1 h, only one layer of Cr_2O_3 is measured.

3. Double dispersive x-ray fluorescence spectroscopy ($D^2\text{XRF}$)

Quantitative analyses of trace and major elements with adjacent fluorescent lines are always a challenge for energy dispersive x-ray Fluorescence (EDXRF) spectrometry. If the absorption edge energy of the trace element surpasses that of the major elements, the inescapable fluorescent emission from the major element could saturate the detector. On the contrary, when the absorption edges of the trace elements fall below those of the major element, the fluorescence of the primary element can be circumvented by selecting an excitation energy that resides within the range defined by the two absorption edges. In this case, Raman scattering is introduced, which can overlap the characteristic lines of the trace element. This can be avoided by using wavelength dispersive XRF, where a crystal analyzer has sufficient energy resolution to separate the neighboring lines of interest. However, this is at the expense of the photon count rate and the detection of only one energy per measurement. This problem has been addressed with our so-called double dispersive XRF ($D^2\text{XRF}$) setup. As shown in Fig. 7, the excitation beam hits the sample, and the fluorescence radiation is detected after being reflected by a crystal. Since the energy of the reflected radiation

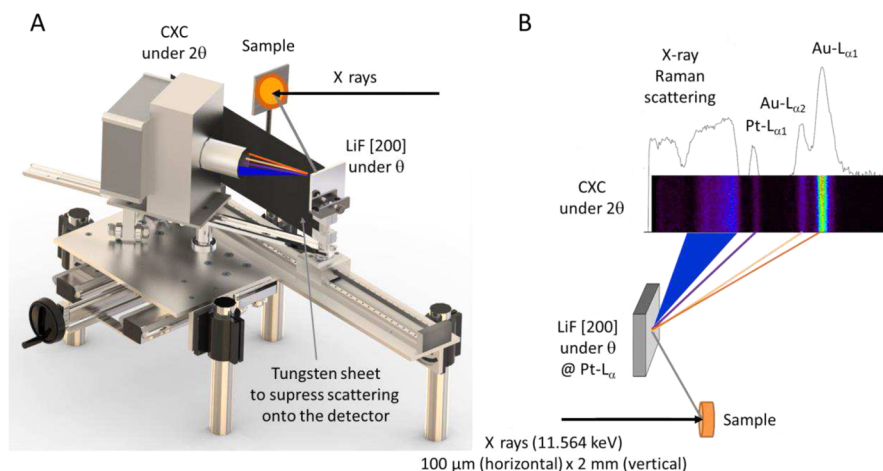


FIG. 7. Scheme of the principle of the $D^2\text{XRF}$ (a). Specific geometry for the case study Pt in Au matrix (b). The exciting monochromatic beam of 11.564 keV is producing Pt-L α fluorescence in the sample (ancient gold artifact). The characteristic radiation is dispersed by a LiF (200) crystal to the detector. The energy resolution of the detector allows us to suppress the background efficiently and to separate the fluorescence line from x-ray Raman scattering [Reproduced with permission from Radtke *et al.*, *Microchem. J.* **125**, 56–61 (2016). Copyright 2016 Elsevier].

depends on the angle, a very simple wavelength dispersive measurement system is realized. In addition to the simple mechanical design, another advantage is that, unlike conventional systems, a wider energy range can be measured simultaneously. The efficient background suppression of the pnCCD and a good energy resolution of the crystal lead to improved limits of detection (LOD) without the need for additional collimators. In first order reflections, an energy resolution of 13 eV for Cu-K α is achieved, and an energy range of 1 keV is covered in one shot.²⁰

In this respect, the determination of platinum (Pt) in ancient gold artifacts has been a very successful application of D²XRF. The presence of Pt in ancient gold objects is one of the most reliable criteria for identifying the alluvial origin of gold. The average amount of Pt in gold alloys gives information about the circulation of the metal in the past.²⁰ In the case of precious, rare, and small museum objects made of gold alloys, the determination of the Pt content must be performed in a non-destructive way. After first attempts to quantitatively determine small amounts of platinum in gold by measuring the gold K-lines⁴⁶ or by modeling the spectra with pure elements,^{47,48} the best results were achieved with the D²XRF. We found mere 0.9 μ g of Pt in 1 g of an alloy with a 99.9% Au matrix.

This setup served originally the purpose of x-ray fluorescence line separation of neighboring elements but is also useful for separating and detecting the low cross-section phenomenon of z-ray Raman scattering (XRRS), as shown in Fig. 7. The high resolving power of the setup enabled the detection of secondary x-ray Raman scattering

effects, which, in turn, opens the capacity to identify low-Z content with the use of hard x rays.⁴⁹

4. Coded aperture x-ray fluorescence spectroscopy (CA-XRF)

Imaging techniques directly deliver an unprecedented level of information about materials' properties, which is easy to interpret. However, imaging techniques for x-ray spectroscopy are limited by the availability of very expensive x-ray optics, such as lenses or capillaries. To remedy this, we developed an imaging technique that does not require lenses: coded aperture XRF (CA-XRF).¹⁹ Coded apertures (CAs) are a simple and cost-effective way of imaging high energy radiation. Conventional pinholes or capillary optics are replaced by a multi-pinhole where the holes can be distributed randomly, or, like in our case, following, e.g., the MURA rules (modified uniformly redundant array).⁵⁰ The image is formed by superimposing the images from each pinhole [Figs. 8(a) and 8(b)]. A reconstruction comparable to that used in computed tomography (CT) is applied to obtain an image of the object under investigation. The advantages are that the achievable count rate scales with the number of holes and that the spatial resolution can be improved by using advanced reconstruction methods. Furthermore, the magnification factor can be easily adjusted by changing the respective distances between the detector, CA, and the imaged object. The resolution of the imaging system depends on the detector pixel size, the hole size of the CA, and the CAs' geometrical arrangement.

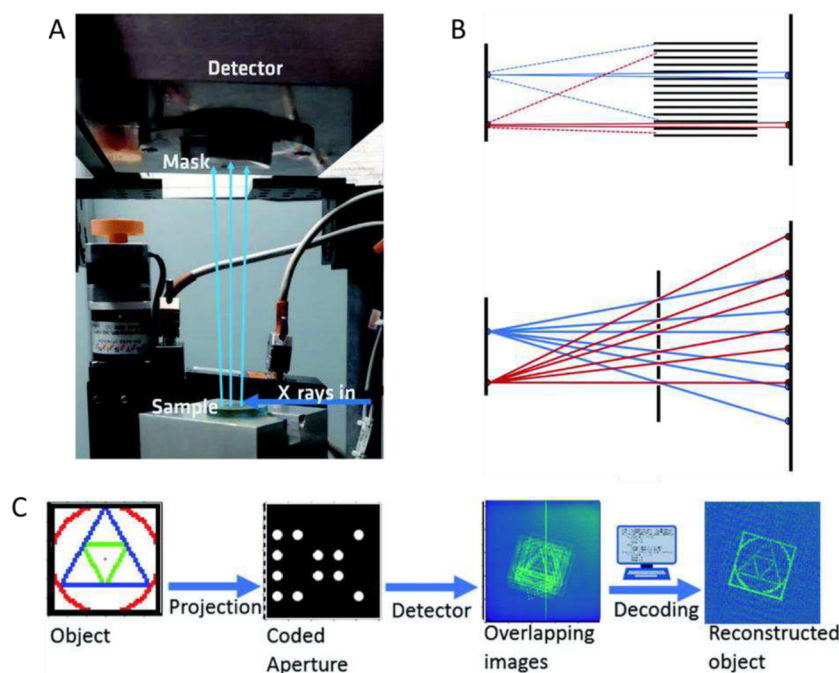


FIG. 8. Overview of coded aperture XRF (CA-XRF) working principle. Setup at the BAMline (a). Principle of different optics: a straight polycapillary optic (top) and a multiple pinhole mask (bottom) (b). Image acquisition procedure from left to right: a sample prepared by drop-on-demand printing—projection of the XRF signal through the mask—image collected by the detector—image reconstruction (c) [Reproduced with permission from Kulow *et al.*, *J. Anal. At. Spectrom.* **35**, 347–356 (2020). Copyright 2020 Royal Society of Chemistry].

Using more than one pinhole can enhance the resolution through the method of multiframe super resolution, described in Ref. 51. This super resolution method is based on the addition of multiple images shifted by a fraction of the detector pixel size, which is actually the case for almost any measurement with multiple pinholes.

We present here a case study of a sample that was prepared via “drop on demand” printing. Further details on this procedure can be found elsewhere.¹⁸ The aim of this experiment was to map

and quantify the distribution of Fe, Co, Ni, Cu, and Sr arranged into specific geometric patterns. The patterns containing the mentioned metal elements were printed on poly(methyl methacrylate) (PMMA) carriers (30 mm diameter, 3 mm thickness) without further modification. The distance between two residues was $\sim 140 \mu\text{m}$. In Fig. 8(c), each color represents a different solution in a different cartridge. The geometric figures do not overlap and have total masses of $25.9 \pm 0.8 \text{ ng Fe}$, $97 \pm 7 \text{ ng Co}$, $44 \pm 3 \text{ ng Ni}$, $56 \pm 4 \text{ ng Cu}$, and $0.26 \pm 0.02 \text{ ng Sr}$. The measurement time was 15 min.

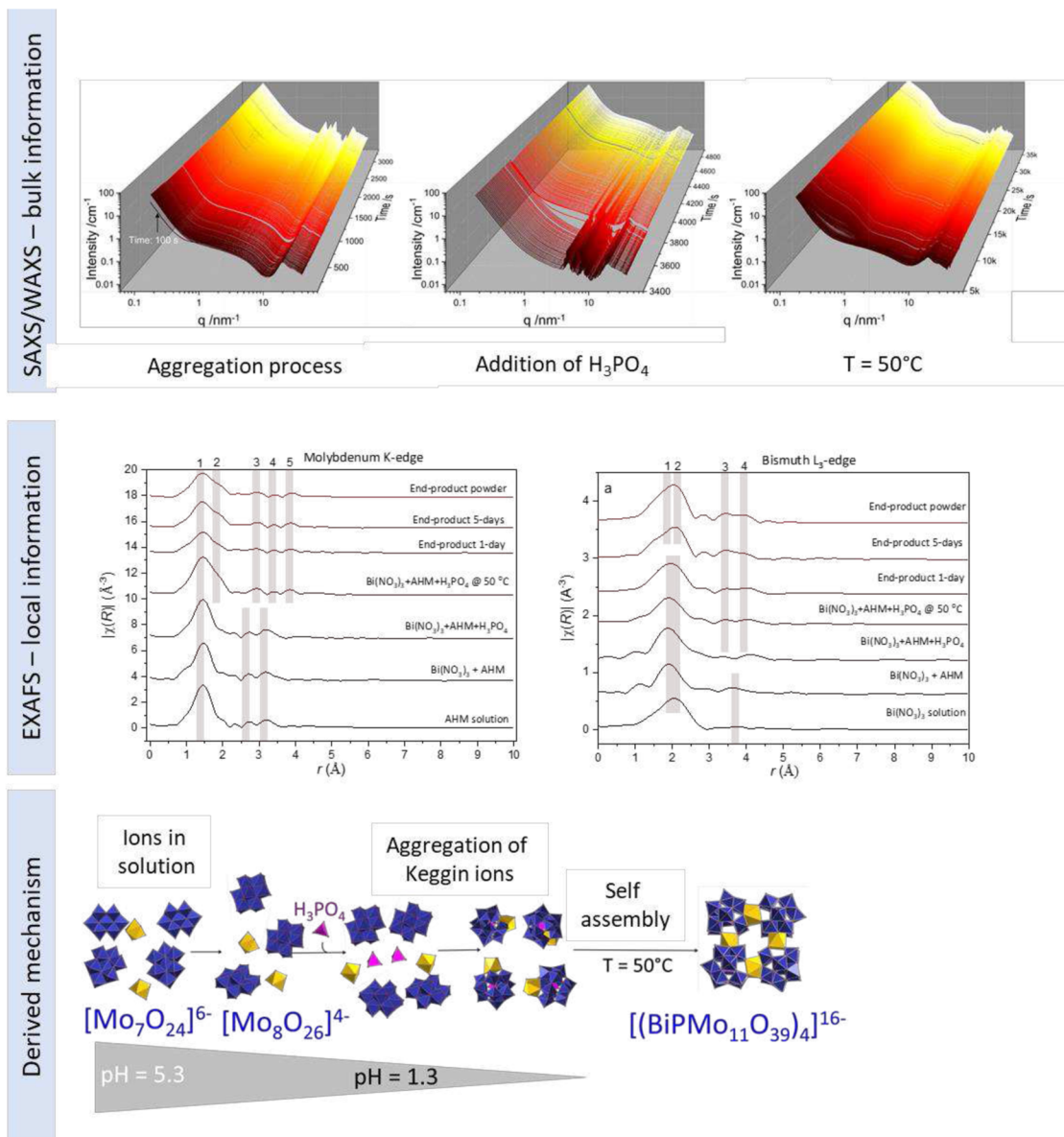


FIG. 9. Investigation of a crystallization with complementary methods on the example of the formation of a polyoxometalate. XAS is advantageous because it can be used to determine the structure of both crystalline and amorphous materials [Reproduced with permission from Martins *et al.*, Chem. Eur. J. **28**, e202200079 (2022). Copyright 2022 Wiley-VCH].

B. Collaborative research

This section is divided either by application or subject area and highlights both material questions and analytical method.

1. Formation mechanisms, synthesis, and clarification

Solution chemistry and early stages of formation of nanostructured phase is an important area of EXAFS' applications in materials chemistry. We highlight a study on the formation and crystallization of Bi-coordinated Keggin-type phosphomolybdate. To elucidate the formation mechanisms, we applied a combination of different analytical techniques, such as time-resolved *in situ* small- and wide-angle x-ray scattering (SAXS/WAXS), but importantly also *in situ* EXAFS measurements on the Mo-K and Bi-L₃ edges (Fig. 9). The overall reaction is relatively slow and involves several sequential synthetic steps. We observed the formation of heteropolyoxometalate (NH₄)₁₆[Bi₄P₄Mo₄₄O₁₅₆] 22H₂O nanorings in aqueous solution, which formed upon mixing of ammonium heptamolybdate with bismuth nitrate in the presence of phosphoric acid at 50 °C.³⁴ Following the reaction using *in situ* EXAFS spectroscopy, characteristic changes in Bi and Mo coordination were detected. All changes were attributed to the formation of Bi-coordinated secondary monomeric building units in solution, followed by their precipitation as amorphous precipitates and further formation of tetrameric nanoring assembling into crystals. EXAFS experiments in solution should be performed using *in situ* cells, allowing for monitoring the reactions, which otherwise typically are performed in batch reactors. For the discussed study, we designed an *in situ* cell with a reaction volume of <15 ml. The cell comprises two Kapton windows for primary and secondary beams and offers a possibility to stir and heat the reagents [Fig. 3(b)]. Kapton windows allow for experiments either in transmission or in reflection, and the cell can be adapted for

x-ray diffraction experiments. Special access ports at the top of the cell can be used for temperature control as well as for adding reactants by means of an automatic syringe pump or manually. An aluminum block was added to facilitate the heat exchange between a stirring hot plate and the reaction cell. The reaction cell was sealed and could be used up to ~180 °C with solutions. Heating and stirring was also controlled remotely. To optimize the beam path for EXAFS measurements, a movable piston was used as the first window, which allowed to adjust the optical beam path from 1 to 40 mm. All the parts were easy to exchange in case of damage, which was important because of potential x-ray flux damage of Kapton windows. Such damage modes are a common case in studies with a high flux beam, white or pink beam, or in studies with dispersive XAFS (see details below).

This usefulness is demonstrated by the application of XAS in studying the development of transition metal phosphates (TMPs), which are becoming increasingly important for electrocatalysis and electrochemistry due to their low cost and tunability. The performance of TMPs depends on their composition [specifically the transition metal cation(s)] as well as their microstructure, such as high surface area and the presence of mesopores. Karafiludis *et al.*⁵² showed that mesoporous TMPs can be made from a precursor metal phosphate phase called M-struvite (NH₄MPO₄·6H₂O, M = Ni²⁺, Co²⁺, Ni_xCo_{1-x}²⁺). This method involves the thermal decomposition of crystalline M-struvite precursors, which convert to an amorphous and mesoporous phase. We observed that very different amorphous and mesoporous, but also crystalline structures could be obtained depending on the involved transition metals, even though the synthesis started with analogous precursor crystals. In particular, we observed a significant change in the pore size and the specific volume during heating depending on whether Ni, Co, or both were present, which was counterintuitive considering just simple evaporation of ammonia and water from NH₄MPO₄·6H₂O.

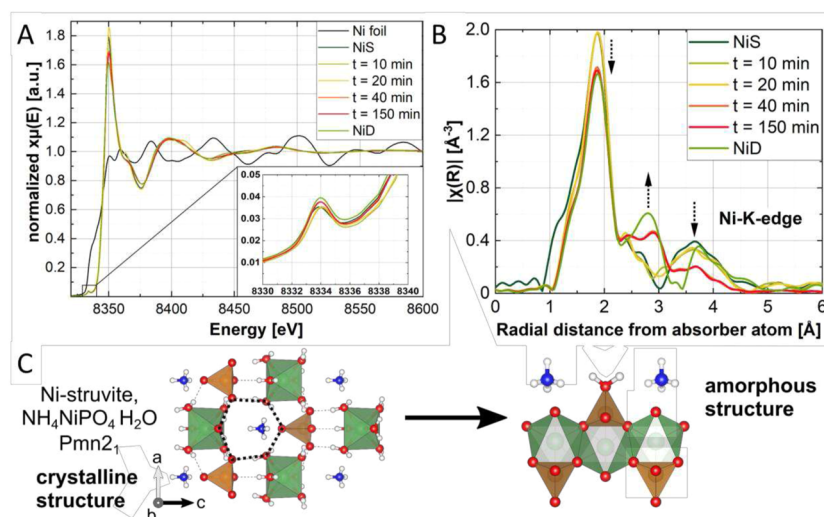


FIG. 10. Normalized XAS spectra of crystalline precursor Ni-struvite (NIS), time series of thermally treated Ni-struvite, and hydrothermally synthesized crystalline Ni-dittmarite (NiD) compared with several M^{2+} ($M = \text{Ni}^{2+}$ and Co^{2+}) standards (only the Ni-foil is shown for clarity) with a detailed view of the pre-peak region (a). Fourier-transformed Ni spectra plotted in the R-space (b). (010) crystal plane of the Ni-struvite structure space group $Pmn2_1$ with the black dashed line of potential near spherical micropores inside the structure and amorphous phase (c) [Reproduced with permission from Karafiludis *et al.*, *Nanoscale* **15**, 3952–3966 (2023). Copyright 2023 Royal Society of Chemistry].

This finding suggested a potential condensation or change in the amorphous structures formed upon heating.

To explain this phenomenon, XAS measurements were performed to characterize the amorphous structure and its correlation with the occurrence of the mesoporous framework (Fig. 10). The selected M-struvites and their decomposition products were measured at the Ni- and Co-edges to compare the distortion of the metal octahedra. This study focused on the intensity of the pre-peak in the XANES region, which indicated the degree of distortion or centrosymmetry around Ni or Co ions. Although both metals initially formed isostructural TMPs, their local coordination environments were different. Ni²⁺ showed nearly ideal octahedral coordination in both the crystalline Ni-struvite (NIS) structure and heated amorphous products, as evidenced by a low pre-peak intensity. In contrast, Co²⁺ showed higher distortion, which increased in heated products. As a result, Ni-struvites decomposed into a single amorphous phase that gradually developed mesoporosity. Conversely, Co²⁺ favored transformation into other crystalline phases, such as Co-dittmarite (NH₄CoPO₄·H₂O), which eradicated any porosity from the material.

2. Compositionally complex materials (CCMats)

Compositionally complex materials and high-entropy alloys with novel properties are investigated as the next generation constructional and functional materials for magnetism, catalysis, energy storage, and energy conversion (see Sec. III A 2).^{53–57} The structure of such compositionally complex materials (CCMats) materials include five major equivalent elemental components, e.g., metal atoms in alloys or metal cations in oxides and nitrides, which are

mixed equimolarly. In other words, CC materials are solid solutions, whose structural homogeneity (the fact of being a solid solution) is verified with x-ray diffraction. However, x-ray diffraction methods traditionally rely on the assumption of a long-range ordering in crystals, and thus, the local structure and local order effects in CCMats are still debated. Consequently, there is a need for element specific techniques to understand ordering/disordering phenomena, which is indeed offered by the x-ray absorption spectroscopy.

The high flexibility of the BAMline allowed us to perform multi-element EXAFS studies on compositionally complex samples. The ability to perform rapid beamline alignments and to change the beamline energy within a few minutes resulted in a relatively efficient use of the instrument, even when several elements had to be studied in one experiment. EXAFS spectra for all five elements in five-component high entropy alloys were collected within a single beam time. For data analysis, we performed simultaneous Reverse Monte Carlo (RMC) modeling of all spectra, which allowed us to obtain not only average interatomic distances and thermal parameters but also characteristic distances for each of the 14 element pairs (Fig. 11).^{58,59} Starting from EXAFS spectra collected for multiple elements, RMC-calculated EXAFS spectra were analyzed using their Fourier and Morlet wavelet transforms. Such an approach was further applied for several high-entropy alloys, such as *fcc*- and *bcc*-structured Al_xCoCrFeNi alloys in a form of homogenized powders, and for *fcc*-CoCrFeNiMn (i.e., the Cantor alloy⁵³) in forms of crystalline bulk samples, powdered alloys, and amorphous thin films.^{54,58,59} In general, as soon as EXAFS spectra for several elements in the material sample had been collected, a single model was applied to all EXAFS spectra. The approach based on reverse

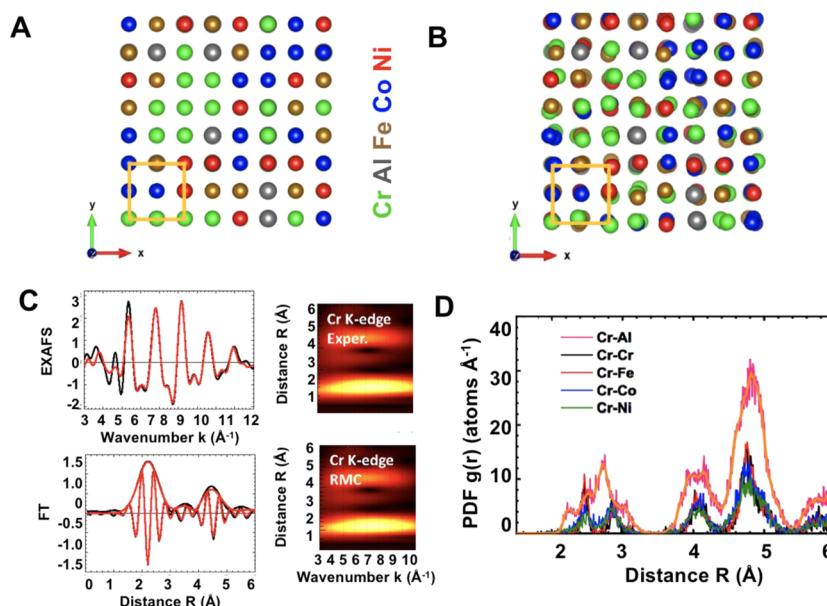


FIG. 11. Atomic structure of HEA generated using RMC for fitting of x-ray absorption spectra (a). Atomic structure of HEA obtained after x-ray absorption spectra fitting (b). Experimental and RMC-calculated Cr K-edge EXAFS spectra $\chi(k) k^2$ (above) and their Fourier and Morlet wavelet transforms (below) for the bcc-structured Al₃-CrFeCoNi HEA at 300 K (c). Chromium-based pair distribution functions $g(r)$ for bcc-structured Al₃-CrFeCoNi HEA extracted from K-edge EXAFS spectra of Cr, Fe, Co, and Ni using the RMC method; orange curve is a linear smoothing (over 13 points) of the PDFs related to Al atoms (d) [Reproduced with permission from Smekhova *et al.*, Nano Res. 15, 4845 (2022). Copyright 2022 Springer].

Monte Carlo fitting proved useful to any complex multicomponent material.^{62,64}

3. Corrosion and other degradation mechanisms

The already mentioned corrosion and degradation studies benefit from the capabilities of a multipurpose materials research beamline. XAS can be used to study the electronic structure of materials that are susceptible to corrosion, such as metals and metal alloys, and can provide information on how to improve their corrosion resistance. Moreover, XRF can be used to study the chemical composition of materials that are susceptible to degradation and can provide information on how to optimize their performance and stability. By understanding the electronic and chemical structure of these materials, the synthesis of materials with improved corrosion resistance and stability can be achieved.

At the BAMline, we have different modes to perform XAS, depending on sample requirements. Sometimes, we need nanometer depth resolution to understand the corrosion mechanisms at the surface level (GE-XAS, described above); in other cases, a high spatial resolution is required to map the degradation/corrosion effects by identifying areal diffusion mechanisms. We review two quite distinct examples: ferritic steel alloys and biological tissues.

Detailed mapping of iron–chrome phases (Fe–Cr) in steel alloys provides information about the formation and diffusion of phases in corrosion layers. Micro-XAS was performed on corroded steel, previously subjected to 650 °C in an atmosphere of 0.2% SO₂. The measurements were performed at the Fe K-edge along the cross section throughout the corrosion layer with a spatial resolution of 2 μm (Fig. 12). Higher iron oxidation states developed from the pure metal toward the outmost layer (surface).²⁷ In this work, both high- and low-steeled alloys were investigated, where a quantitative identification of phases throughout the cross section was obtained. Further development of corrosion research requires sample environment for *in situ* studies of alloys under heating as well as chemical impact. For this purpose, we developed a dedicated chamber for XAS measurement in a fluorescence mode upon heating up to 600 °C under reactive atmosphere, such as air, pure O₂, or SO₂.

Degradation mechanisms are also a major concern in biomedicine, especially if the use of implants is necessary. For instance, the abrasion and degradation of implants can become

a serious health hazard due to the contamination of tissues by metal ions. In collaboration with the University Medical Center Hamburg-Eppendorf (UKE), the cobalt deposition in periprosthetic bone specimens was studied in undecalcified histological thin sections. We determined cobalt accumulations in the bone matrix. We also showed for the first time via synchrotron XRF with a high spatial resolution and directly on histological slides that cobalt deposits in the mineralized bone matrix in a mineral-specific way. The extent of this deposition is dependent on the implant lifetime.¹² Due to the increasing numbers of implant revisions, this is a current clinical issue. It can lead to patient discomfort, prolonged recovery time, and increased healthcare costs. Interactions of the endoprosthesis biomaterial with the body affect implantation time by wear processes, i.e., corrosion and abrasion. Previously, cobalt–chrome implants were shown to cause high levels of cobalt ions deposited in the bone matrix. To determine the potential functional role of these ions in bone homeostasis, we developed a non-destructive dual analysis of highly sensitive elemental analysis by synchrotron XRF directly in undecalcified histological bone thin sections (4 μm). In this study, 28 bone samples from hip endoprosthesis carriers (surface replacement arthroplasty, metal-on-metal bearing) with an implant lifetime of 17–1750 days were used. Results were compared with age-matched control specimens. The histological analysis identified areas of bone cell activity and assigned them for further XRF measurements. Co–Cr wear particles were identified in the bone marrow. In addition, Co ions were highly enriched in the mineralized bone matrix. The cobalt deposits were not homogeneously distributed, and areas of high signal intensity were identified. Co was distinctly deposited in the newly formed osteoid layer but also within deeper layers of the bone matrix, whereby the Co concentration increased with higher degrees of bone matrix mineralization. An example of this is shown in Fig. 13.

The examination of liver cells from Wilson's disease (WD) patient was another application of XRF, which we conducted together with colleagues from the University of Münster.²⁸ WD is a rare genetic disorder, which means 1 in 30 000 people is affected. It is an autosomal recessive inherited disease resulting in Cu accumulation, caused by a defective gene ATP7B. It shows numerous and often unspecific symptoms and is difficult to diagnose due to the many different symptoms. One of its effects is the accumulation of Cu in the liver and central nervous system.

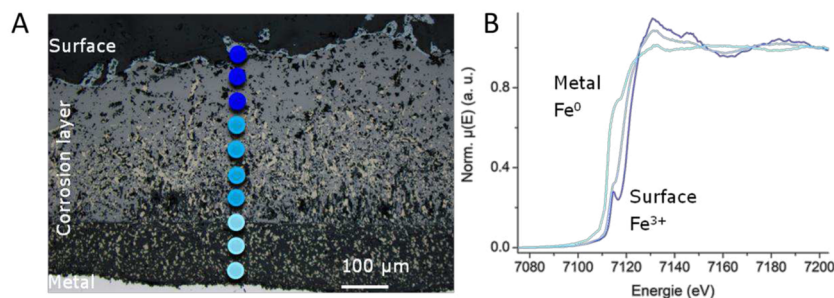


FIG. 12. Identification of corrosion phases in high-alloyed steel with micro-XAS. Corrosion layer of Fe2Cr alloy previously submitted to 650 °C and 0.2% SO₂ atmosphere (a). XAS Spectra at the Fe–K edge acquired with a spatial resolution of 2 μm (b). Higher Iron oxidation states are developed from the pure metal toward the outmost layer (surface).²⁷

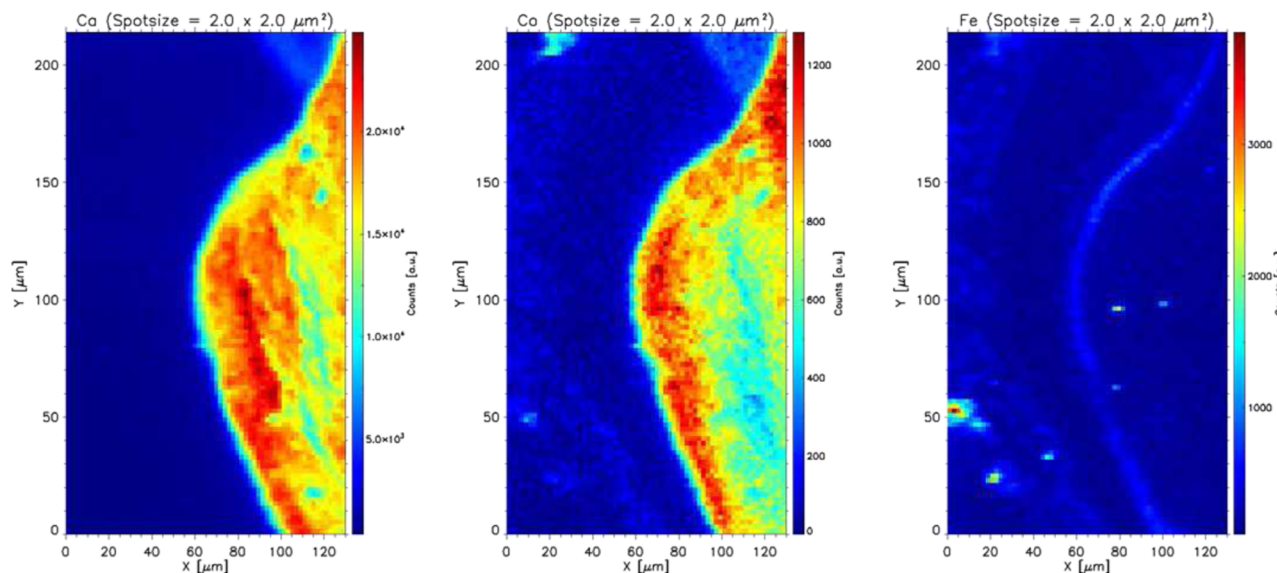


FIG. 13. The mapping of the Ca concentration shows the mineralized bone. The Co concentration is higher in the outer (newer) zone of the bone. This indicates that the Co was embedded during the bone growth process. The higher Fe level in the growth zone indicates increased blood circulation [Reproduced with permission from Hahn *et al.*, *Materialia* **6**, 100290 (2019). Copyright 2019 Elsevier].

A liver biopsy specimen from a WD patient was analyzed using micro-XRF spectroscopy to determine the elemental distribution. First, benchtop micro-XRF was utilized for the determination of a region of interest (ROI) for further analysis. To obtain detailed elemental information, this ROI was analyzed by synchrotron radiation-based micro-XRF at the BAMline with a beam size of 4 μm offering a resolution at the length-scales of cells and comparable to that of optical microscopy. Distribution maps of additional elements, such as copper (Cu), iron (Fe), zinc (Zn), and

manganese (Mn), were obtained, thanks to a higher sensitivity of SR-micro-XRF (Fig. 13).

In the WD sample, a Cu accumulation at the outer sphere of hepatocytes and a Fe accumulation within the hepatocytes were detected. For the control samples, a homogeneous Cu distribution was found. Additionally, for the WD sample, the copper concentrations were higher than in the control sample. Further investigations regarding the oxidation state of Cu were also carried out.

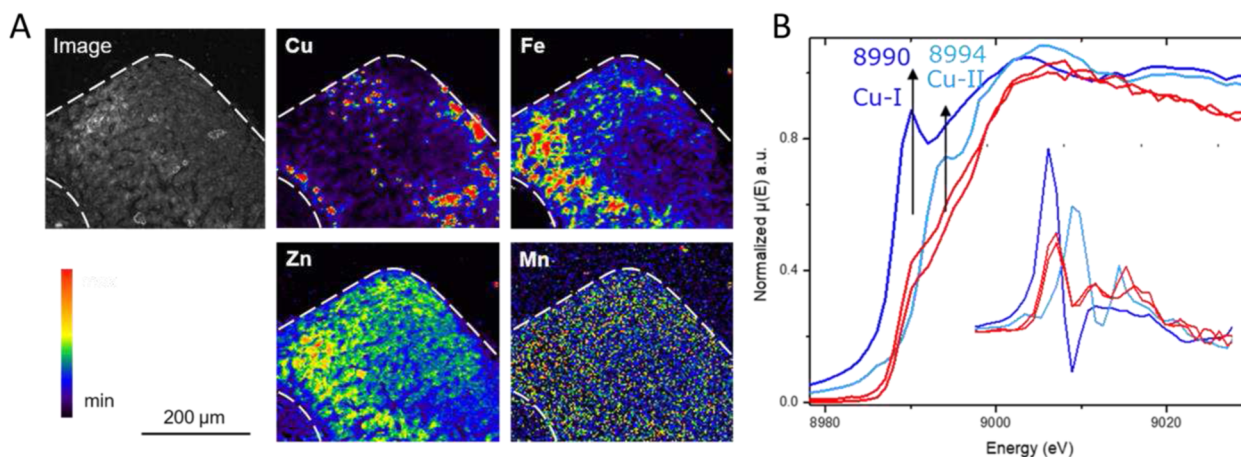


FIG. 14. Autofluorescence microscopic image of the WD liver sample investigated by bench-top micro-XRF, distribution maps of Cu, Fe, Zn, and Mn (a). An inverse correlation between Cu and Fe is detected. In addition to this, Zn is showing a similar distribution pattern as Fe and correlates inversely with Cu. The three elements Cu, Fe, and Zn reveal an elevated intensity within the hepatocytes in comparison to the surrounding liver tissue. Cu K-edge XANES (red) together with Cu(I) (light blue) and Cu(II) (dark blue) standards (b) [Reproduced with permission from Hachmüller *et al.*, *Metallomics* **8**, 648–653 (2016). Copyright 2016 Royal Society of Chemistry²⁸].

XRF and XAS used for medical samples give information not only about elemental distribution in tissues, bones, or model organisms but also extended chemical information about the chemical nature of bioinorganic species. Parallel to the elemental distribution in Morbus-Wilson disease representative tissues, the XANES study was carried out at the Cu K-edge (8.979 keV) on two areas with a higher concentration of Cu (Fig. 14), previously identified by XRF. It was shown that Cu in the sample existed as a mixture of both Cu(I) and Cu(II) species.⁵⁰

4. Batteries, energy storage devices, and catalysis

Energy storage applications can also benefit from the capabilities of the multi-purpose materials research beamline. XAS can be used to study the electronic structure of materials used in batteries, such as lithium-ion batteries, and provide information on how to

improve their performance and longevity. In addition, XRF can be used to study the chemical composition of materials used in energy storage devices, such as supercapacitors, and provide information on how to optimize their performance and stability. By understanding the electronic and chemical structure of these materials, the synthesis of better energy storage materials can be achieved. Research at the BAMline has made significant contributions to a wide range of topics, such as energy storage, batteries, and catalysis.^{9,28,63–68} Below, we highlight some recent case studies.

Electrocatalytically active pyrrolic FeN₄ sites in Fe–N–Cs are considered vital to replace the expensive precious group metal-based materials (PGMs). These nano-architectures are challenging for structural characterization and require a combination of methods.⁶³ EXAFS studies can solve the structure only in combination with complementary techniques. To characterize Fe active sites, EXAFS

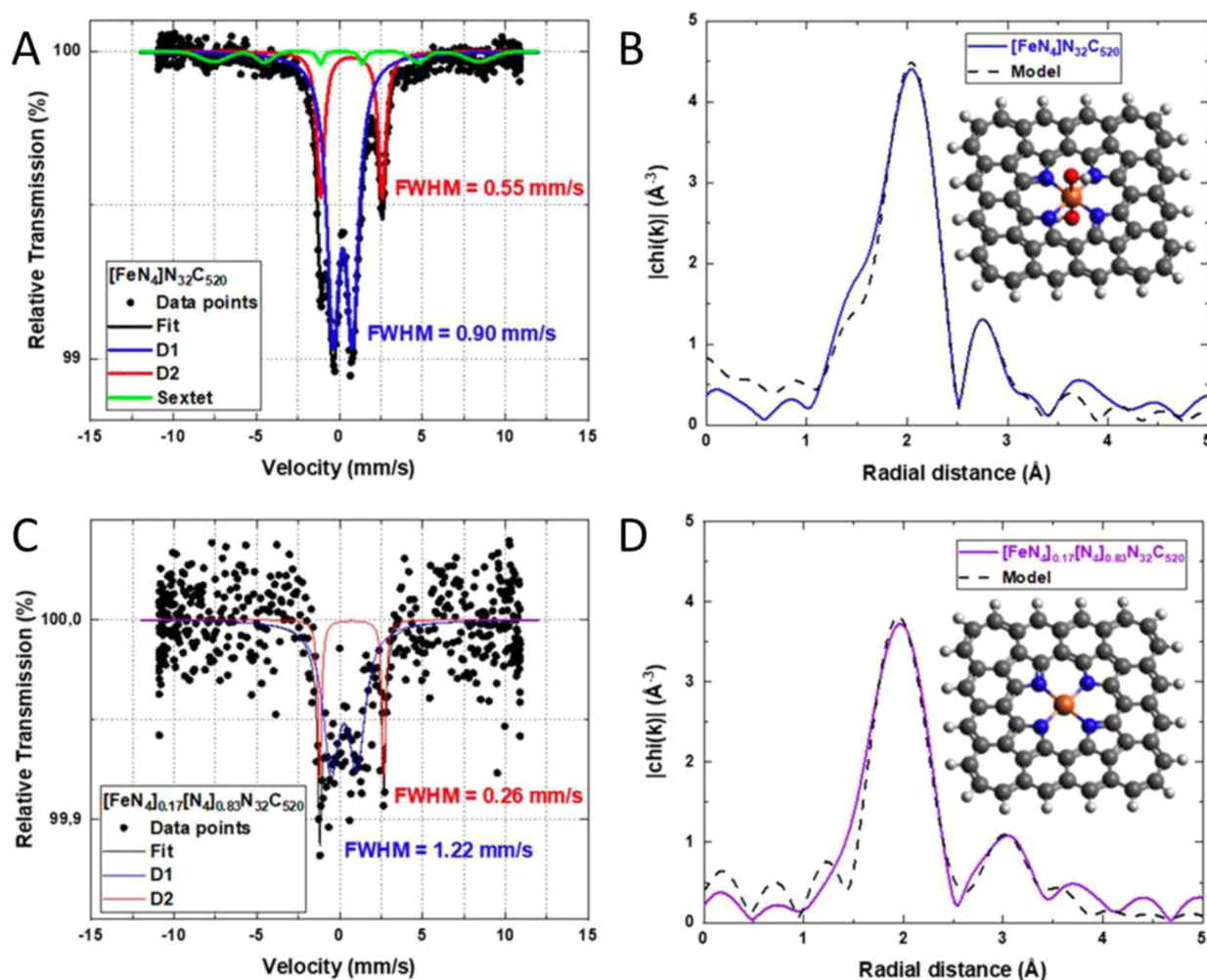


FIG. 15. Characterization of the Fe environment of (a) and (b) [FeN₄]N₃₂C₅₂₀ and (c) and (d) [FeN₄]_{0.17}[N₄]_{0.83}N₃₂C₅₂₀. (a)–(c) Mössbauer spectrum measured at 4.2 K; FWHM indicates the linewidth of the corresponding quadrupole doublet. (b) and (d) Experimental Fourier transform of the Fe K-edge EXAFS spectra and best fit EXAFS model using the structure displayed in the corresponding inset (orange = Fe, blue = N, red = O, gray = C, and white = H) [Reproduced with permission from Menga *et al.*, *Angew. Chem., Int. Ed.* **61**, e202207089 (2022). Copyright 2022 Wiley].

in standard mode was combined with Mössbauer-spectroscopy to obtain a reliable model. A very good agreement with the model based on a 2D tetrapyrrolic Fe–N–C (Fig. 15) allowed to extract all structural parameters characteristic for the composite material and prove the formation of Fe–N–Cs with Fe cations coordinated to four pyrrolic N at 2.04 Å and ≈ 1 O atoms (from axial OH ligands) at 1.83 Å.

With the help of a custom-built electrochemical cell for *in situ* XAS measurements [Fig. 3(a)], it was possible to follow the chemical entities (H, O, H_2PO_4^- , and H_3PO_3) adsorbed on the Pt nanoparticle catalyst at different potentials under the oxygen reduction reaction conditions in several electrolytes (HClO_4 , H_3PO_4 , and H_3PO_3). Based on the analysis of the Pt L_3 absorption edge, it was found that H_3PO_3 adsorbs $\text{P}(\text{OH})_3$ in a pyramidal configuration via a Pt–P bond (Fig. 16). The competition between the adsorption of H_3PO_4 and H_3PO_3 allowed for a better understanding of the mechanism of catalyst formation and helped to develop strategies for minimizing H_3PO_3 formation.

In catalysis, XAS is used to study the electronic structure of catalytic materials, such as metal nanoparticles and metal-organic frameworks. This information is important to optimize the performance and the synthesis of these materials and improve their efficiency in catalytic reactions. Additionally, XRF can be used to study the chemical composition of catalytic materials at their microstructure level and in combination with XAS provide information on how to optimize their performance and stability. The complementary aspects of XAS and XRF have been demonstrated in studies of batteries and fuel cells, particularly in the case of the vanadium redox flow battery (VRFB), which is a promising technology for stationary energy storage. To avoid capacity degradation in VRFBs, it is crucial to understand the fundamental diffusion mechanisms and transport of vanadium in the membranes. Micro-XAS measurements were recently performed on Nafion 117 membranes and revealed significant differences in the diffusion coefficient for the different vanadium species and the influence of different transport mechanisms. These differences have been attributed to reactions occurring within the membrane. To test this hypothesis, it was investigated whether redox reactions occur within the nanoscopic water body of Nafion 117 as well as in novel polyvinylidene fluoride (PVDF)-based membranes. X-ray absorption near-edge structure (XANES) spectroscopy was used to distinguish between the different vanadium

species, including V^{3+} , VO^{2+} , and VO_2^+ , inside hydrated Nafion 117 and PVDF-based membranes (Fig. 17). The results shed light on the complex transport behavior of vanadium ions within the membranes and provide insight into the underlying mechanisms contributing to the discrepancies observed in previous models.⁶⁷

IV. OUTLOOK

A. Data science and machine learning for BAMline: The future of x-ray research at BAMline

Future measurement strategies at the synchrotrons will involve dynamic, time-resolved methods, producing increasingly more and more data. This progress relies on new detectors and data evaluation methods. These two factors in conjunction with an associated data storage requirements are major challenges and opportunities at the same time. The implementation of machine learning (ML) will provide new data interpretation possibilities, particularly when combined with multimodal measurements for analyzing materials at different scales. Treating these points and trends as genuine scientific questions is crucial.

Although the BAMline has proven to be powerful for studying matter, it still poses challenges in data acquisition, processing, analysis, and interpretation. Novel data science methods and techniques offer solutions, and we have begun implementing them throughout the BAMline experimental workflow: from the planning stage to the beamline alignment and measurement processes, all the way to the data evaluation phase.

The first step for a successful experiment is to confirm the beamline's capabilities, such as energy range, flux, resolution, and polarization. To help with this, we have started to install a digital twin on the base of the XRT x-ray tracer for enhanced monitoring, simulation, and optimization.⁶⁹ The XRT (XRyTracer)⁷⁰ is a Python software library for ray tracing and wave propagation in an x-ray regime. It can model synchrotron sources, beamlines, and their elements with high accuracy and flexibility. When the implementation is finished, the digital twin based on XRT can simulate the behavior of the used x-ray optics and detectors under different conditions and configurations. Figure 18 illustrates the beam size impact on energy resolution dE/E , essential for XANES measurements. For example, with a Si111 DCM and 1 mm vertical aperture, dE is 1.2 eV FWHM at Cu K edge 8.979 keV; with 3 mm, it is 3 eV. The

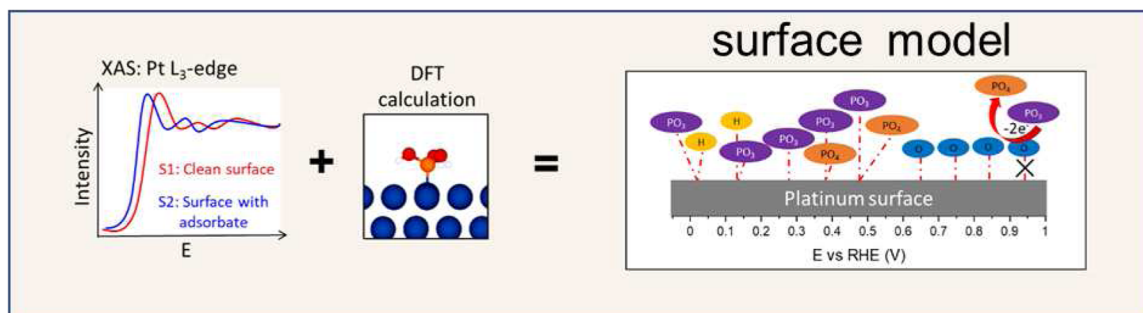


FIG. 16. *In situ* tests were performed on the Pt L_3 edge for different voltages and electrolytes (surface with adsorbate). DFT calculations could prove different adsorption structures on Pt(111) surfaces. [Reproduced with permission from Gomes *et al.*, ACS Catal. 12, 11472–11484 (2022). Copyright 2022 American Chemical Society].

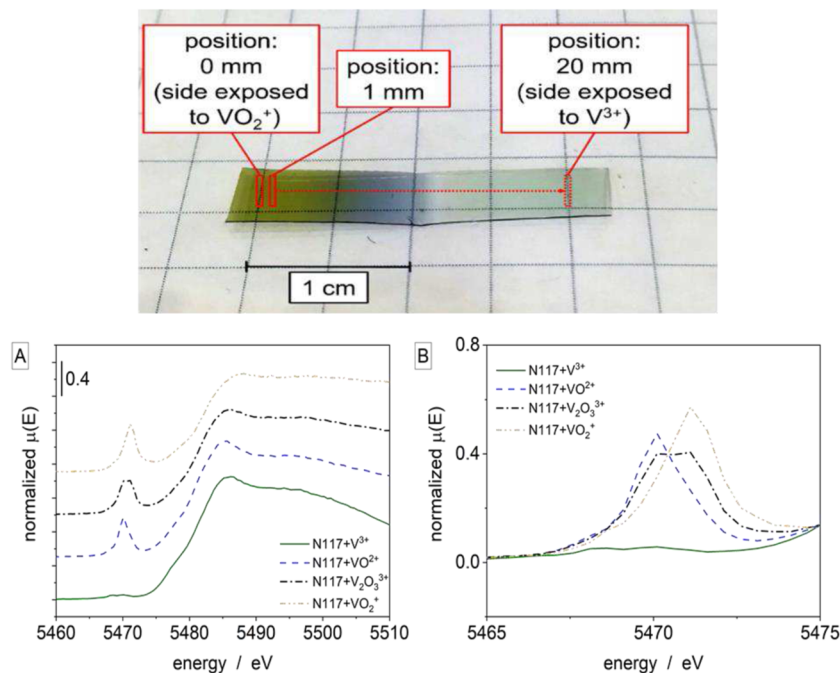


FIG. 17. Top: Nafion 117 exposed to VO_2^+ from the left (0 mm) and to V^{3+} from the right side (20 mm) after six days in the desiccator and 18 days in a sealed polyethene bag. Bottom: XANES at the V K-edge of Nafion 117 hydrated with 1.6M V^{3+} , VO_2^+ , $\text{V}_2\text{O}_3^{3+}$, and VO_2^+ electrolyte for 72 h (a). Highlight of the pre-peak region for all spectra (b) [Reproduced with permission from Lutz *et al.*, J. Power Sources **483**, 229176 (2021). Copyright 2021 Elsevier⁷⁰].

digital twin is anticipated to offer real-time beamline performance monitoring by integrating EPICS control, allowing comparison of experimental parameters and swift identification of discrepancies, resulting in efficient and accurate experiments.

The proper alignment of all components is a crucial step during the actual experiment. This can be challenging due to the large number of parameters involved.⁷¹ For instance, XANES requires the alignment of both DMM and DCM, which together have ~ 10 motor

positions that need to be optimized. Although some of them are less critical, at least the angle of the second multilayer and the pitch angle of the second DCM crystal are essential for achieving optimal results. Moreover, changes in the electron beam orbit and other deviations from ideal conditions may affect the flux significantly. Therefore, it is advisable to optimize not only those parameters but also the positions of apertures as well as vertical translations of crystals and multilayers. To support the user with this task, a program based on

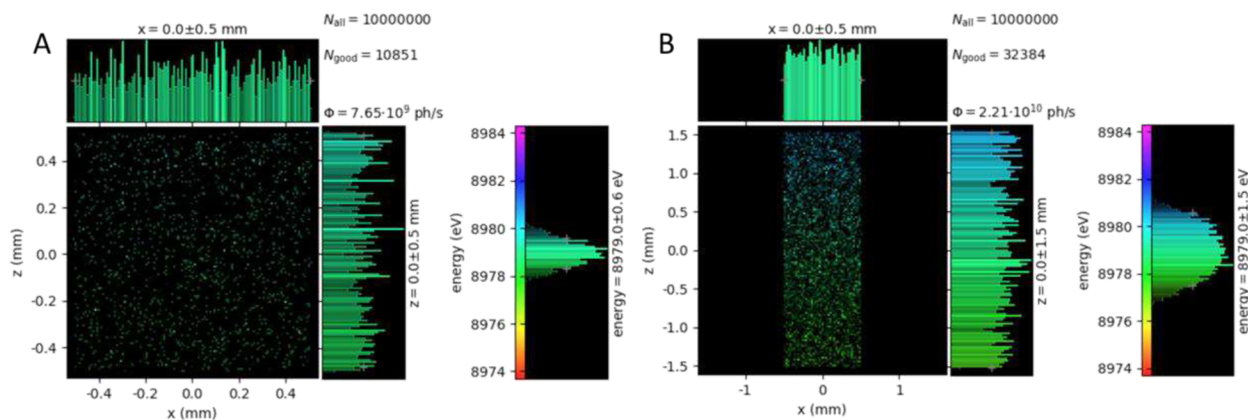


FIG. 18. The distribution of photons after the last aperture. On the left with a vertical aperture of 1 mm and on the right with a vertical aperture of 3 mm. The influence of the beam size on the energy resolution is visible. Calculations are based on the XRT toolkit. Source: own research.

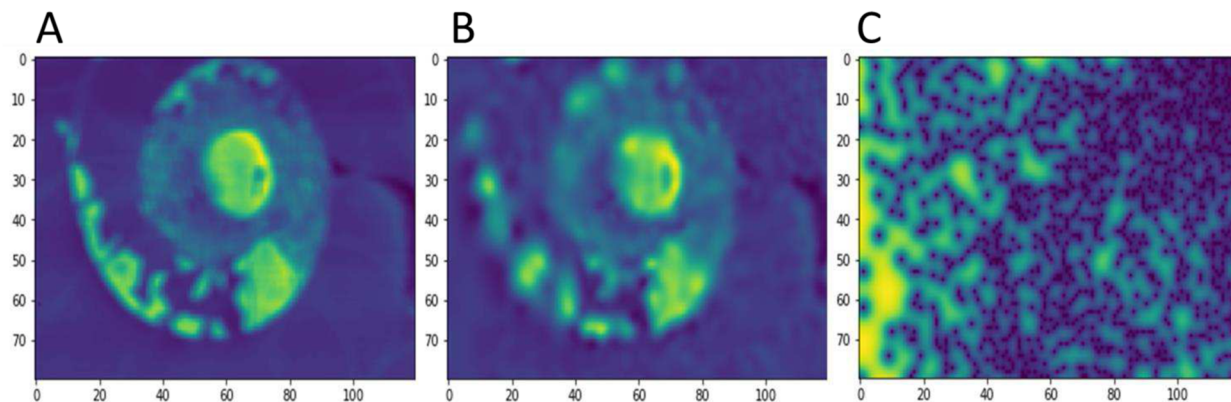


FIG. 19. Results of a step scan with 8991 points (a). Results of a Bayesian scan with 2466 points (b). The image quality is comparable, and the uncertainty information is an additional benefit (c).

Bayesian optimization with Gaussian processes with a user-friendly Graphical User Interface (GUI) was developed. Bayesian optimization⁷⁰ is a method for finding the optimal value of a computationally expensive, or time-consuming to evaluate, black-box function by using a probabilistic model to guide the search. Gaussian processes are a common choice for modeling the function as they provide a flexible and nonparametric way to represent uncertainty over functions.⁷³ Gaussian processes are defined by a mean function and a covariance function, which encode prior assumptions about the function's behavior. Bayesian optimization can handle noise, complex functions, and high-dimensional inputs and provide confidence intervals but is computationally expensive for large datasets. Traditional scans or grid searches are impractical due to time constraints at beamlines. The Bayesian method, taking only 10 min and yielding a 5% higher flux than manual optimization, simplifies the process by specifying the parameter range and automating probing points.

Bayesian optimization can also optimize sample scanning for optimal information within a limited time. Standard techniques, such as 2D step scans, have downsides, for instance, a large number of points and inflexible step sizes. Continuous scanning schemes and elaborate tracks reduce the time needed but can still be improved. Using Bayesian approaches, points are selected to maximize information gain. Figure 19 compares two scans: one with 8991 points and another with 2466 optimized points, both showing an ammonite. Despite a threefold reduction in points, the optimized scan yields a comparable image with the added benefit of measurement uncertainty information.

Another technique where this method was applied is GXANES. In this case, the needed time was reduced by a factor of 10. Taking this approach further, one can encode the desired information into the selection function for the points to measure, e.g., to decide which hypothesis is correct with a minimum number of measurements.⁷⁴

In the evaluation of the data obtained from measurements, various procedures based on artificial neural networks (ANNs) have been developed until now. As an example, we employed ANNs for the reconstruction of the coded aperture measurements. In our previous work,¹⁹ we described three reconstruction methods based on

deconvolution, iterative algorithm, and a neural network. We used a mixed-scale dense convolutional neural network for image reconstruction with a machine learning algorithm. The training data were generated by convolving input images with the projected mask pattern, and careful selection of training input data was shown to be crucial for achieving good results. The trained network was able to reconstruct images in milliseconds, which is significantly faster than the conventional methods that take a few minutes up to an hour. However, significant effort and time are required to produce adequate training samples and to train the network. We proposed to overcome these challenges by training ANNs on simulated data generated by Monte Carlo methods, as we used this approach to improve SR-XRF data analysis.⁷⁵

A new motorized x-ray zoom lens, developed by the Karlsruhe Institute of Technology's Institute for Microstructure Technology (KIT/IMT),⁷⁶ will be integrated and tested at the BAMline. This lens is based on an adjustable number of polymer compound refractive x-ray lenses (CRLs). It offers a wide range of photon energy along with easy lens reconfiguration and adjustable spot sizes, enhancing the efficacy of x-ray fluorescence (XRF) measurements and the selection of absorption edge for XAS studies. The lens's unique capability to perform hierarchical scanning with variable spot sizes on sample surfaces augments its application to a variety of hierarchical materials, including wood and teeth. This pioneering tool, apart from facilitating XRF mapping and micrometer-resolved XANES and EXAFS, will significantly diversify the repertoire of beamline methods, paving the way for an expanded research scope.

V. CONCLUSION

The BAMline has a long and successful history in materials characterization. As a multi-purpose beamline, the BAMline covers XRF, XAS, and hard x-ray imaging. In this article, we have highlighted the capabilities of the BAMline to probe the electronic and chemical structure of materials. The versatile techniques span a range of disciplines, including materials science, chemistry, biology, medicine, and cultural heritage. In the future, the BAMline will

continue to play a crucial role in assessing the properties of materials and their performance in various applications. We are delighted that our research contributes to the development of materials and addresses some of the world's most pressing challenges. Further developments at the BAMline will include improvements in both electronics and software to provide users with a stable beam of different sizes and energies suitable for a wide range of applications, including time and space-resolved studies. Further intensive development of user-friendly semi-automatic control and data reduction software based on advanced artificial intelligence algorithms will keep the BAMline among the leading universal beamlines available for user experiments.

ACKNOWLEDGMENTS

We would like to express our deepest gratitude to HZB for providing access to synchrotron radiation at BESSY and for fostering our collaboration over two decades. We would also like to thank all the users who have used the BAMline and all the former staff and the master and Ph.D. students who have contributed tirelessly to the work on the BAMline. Their contributions have had a significant impact on the success of our research and have enabled us to continue to push the boundaries of our knowledge. We thank Dr. Heinrich Riesemeier for his dedication and many years of support and contribution to further developments at the BAMline.

It is with great sadness that we dedicate this manuscript to the memory of Dr. Uwe Reinholz (1956–2022), an esteemed colleague and scientist. Uwe's contributions to our work went far beyond the scope of this project. His expertise, dedication, and commitment to science were an inspiration to all of us who had the privilege of working with him.

AUTHOR DECLARATIONS

Conflict of Interest

The authors have no conflicts to disclose.

Author Contributions

Ana Guilherme Buzanich: Conceptualization (equal); Formal analysis (equal); Investigation (equal); Methodology (equal); Supervision (equal); Visualization (equal); Writing – original draft (equal). **Martin Radtke:** Conceptualization (equal); Formal analysis (equal); Investigation (equal); Methodology (equal); Supervision (equal); Writing – original draft (equal). **Kirill V. Yusenko:** Conceptualization (equal); Formal analysis (equal); Investigation (equal); Methodology (equal); Writing – original draft (equal). **Tomasz Stawski:** Conceptualization (equal); Formal analysis (equal); Methodology (equal); Writing – original draft (equal); Writing – review & editing (equal). **Anicó Kulow:** Formal analysis (equal); Investigation (equal); Software (equal); Writing – review & editing (equal). **Cafer Tufan Cakir:** Formal analysis (equal); Investigation (equal); Software (equal); Validation (equal). **Bettina Röder:** Visualization (equal). **Christoph Naese:** Visualization (equal). **Ralf Britzke:** Validation (equal); Writing – review & editing (equal). **Michael Sintschuk:** Validation (equal); Writing – review & editing

(equal). **Franziska Emmerling:** Conceptualization (equal); Methodology (equal); Resources (equal); Supervision (equal); Visualization (equal); Writing – original draft (equal); Writing – review & editing (equal).

DATA AVAILABILITY

Data sharing is not applicable to this article as no new data were created or analyzed in this study.

REFERENCES

- ¹W. Görner *et al.*, “BAMline: The first hard X-ray beamline at BESSY II,” *Nucl. Instrum. Methods Phys. Res., Sect. A* **467–468**, 703–706 (2001).
- ²H. Markötter, M. Sintschuk, R. Britzke, S. Dayani, and G. Bruno, “Upgraded imaging capabilities at the BAMline (BESSY II),” *J. Synchrotron Radiat.* **29**, 1292–1298 (2022).
- ³H. Riesemeier *et al.*, “Layout and first XRF applications of the BAMline at BESSY II,” *X-Ray Spectrom.* **34**, 160–163 (2005).
- ⁴V. M. Borovikov *et al.*, “Superconducting 7T wave length shifter for BESSY-II,” *Nucl. Instrum. Methods Phys. Res., Sect. A* **467–468**, 181–184 (2001).
- ⁵F. Schäfers and M. Krumrey, “REFLEC-A program to calculate VUV and soft x-ray optical elements and synchrotron radiation beamlines,” *Technischer Bericht BESSY TB 201*, 1996, pp. 1–17.
- ⁶G. Buzanich, M. Radtke, U. Reinholz, H. Riesemeier, and C. Strel, “Micro-X-ray absorption spectroscopy with compound refractive lenses,” *J. Anal. At. Spectrom.* **27**, 1803 (2012).
- ⁷S. Karafiludis *et al.*, “Ni- and Co-struvites: Revealing crystallization mechanisms and crystal engineering toward applicational use of transition metal phosphates,” *Cryst. Growth Des.* **22**, 4305–4315 (2022).
- ⁸P. F. M. de Oliveira *et al.*, “Tandem X-ray absorption spectroscopy and scattering for *in situ* time-resolved monitoring of gold nanoparticle mechanosynthesis,” *Chem. Commun.* **56**, 10329–10332 (2020).
- ⁹B. F. Gomes *et al.*, “Following adsorbed intermediates on a platinum gas diffusion electrode in H₃PO₃-containing electrolytes using *in situ* X-ray absorption spectroscopy,” *ACS Catal.* **12**, 11472–11484 (2022).
- ¹⁰A. Guilherme Buzanich *et al.*, “Dispersive x-ray absorption spectroscopy for time-resolved *in situ* monitoring of mechanochemical reactions,” *J. Chem. Phys.* **157**, 214202 (2022).
- ¹¹O. Reifschneider *et al.*, “Revealing silver nanoparticle uptake by macrophages using SR- μ XRF and LA-ICP-MS,” *Chem. Res. Toxicol.* **33**, 1250–1255 (2020).
- ¹²M. Hahn, G. Buzanich, K. Jähn, U. Reinholz, and M. Radtke, “Analysis of cobalt deposition in periprosthetic bone specimens by high-resolution synchrotron XRF in undecalcified histological thin sections,” *Materialia* **6**, 100290 (2019).
- ¹³M. Rauwolf *et al.*, “Synchrotron radiation micro X-ray fluorescence spectroscopy of thin structures in bone samples: Comparison of confocal and color X-ray camera setups,” *J. Synchrotron Radiat.* **24**, 307–311 (2017).
- ¹⁴J. F. Curado *et al.*, “ μ -SRXRF characterization of Brazilian emeralds,” *J. Phys.: Conf. Ser.* **499**, 012016 (2014).
- ¹⁵R. Margreiter *et al.*, “Investigations on fire-gilding,” *Archaeometry* **64**, 1465–1478 (2022).
- ¹⁶G. Buzanich *et al.*, “Impurities in multicrystalline silicon wafers for solar cells detected by synchrotron micro-beam X-ray fluorescence analysis,” *J. Anal. At. Spectrom.* **27**, 1875 (2012).
- ¹⁷A. R. Cabral *et al.*, “Iodine in alluvial platinum–palladium nuggets: Evidence for biogenic precious-metal fixation,” *Chem. Geol.* **281**, 125–132 (2011).
- ¹⁸A. Kulow, A. Guilherme Buzanich, U. Reinholz, C. Strel, and M. Radtke, “On the way to full-field X-ray fluorescence spectroscopy imaging with coded apertures,” *J. Anal. At. Spectrom.* **35**, 347–356 (2020).
- ¹⁹A. Kulow *et al.*, “Comparison of three reconstruction methods based on deconvolution, iterative algorithm and neural network for X-ray fluorescence imaging with coded aperture optics,” *J. Anal. At. Spectrom.* **35**, 1423–1434 (2020).

- ²⁰M. Radtke *et al.*, “Double dispersive X-ray fluorescence (D²XRF) based on an energy dispersive pnCCD detector for the detection of platinum in gold,” *Microchem. J.* **125**, 56–61 (2016).
- ²¹M. Radtke, U. Reinholz, and R. Gebhard, “Synchrotron radiation-induced X-ray fluorescence (SRXRF) analyses of the Bernstorf gold,” *Archaeometry* **59**, 891–899 (2017).
- ²²M. F. Guerra, E. Neri, and M. Radtke, “Gold leaf tesserae: Tracing the origins of gold using synchrotron-based techniques,” *Eur. Phys. J. Plus* **138**, 127 (2023).
- ²³I. Tissot *et al.*, “A multi-analytical approach to gold in Ancient Egypt: Studies on provenance and corrosion,” *Spectrochim. Acta, Part B* **108**, 75–82 (2015).
- ²⁴M. Radtke *et al.*, “Slicing—A new method for non destructive 3D elemental sensitive characterization of materials,” *J. Anal. At. Spectrom.* **29**, 1339–1344 (2014).
- ²⁵F. Förste *et al.*, “Quantitative analysis and 2D/3D elemental imaging of cocoa beans using X-ray fluorescence techniques,” *Anal. Chem.* **95**, 5627–5634 (2023).
- ²⁶B. De Samber *et al.*, “Three-dimensional X-ray fluorescence imaging modes for biological specimens using a full-field energy dispersive CCD camera,” *J. Anal. At. Spectrom.* **34**, 2083–2093 (2019).
- ²⁷K. Weber, A. Guilherme Buzanich, M. Radtke, U. Reinholz, and C. Stephan-Scherb, “A μ -XANES study of the combined oxidation/sulfidation of Fe–Cr model alloys,” *Mater. Corros.* **70**, 1360–1370 (2019).
- ²⁸O. Hachmüller *et al.*, “Elemental bioimaging and speciation analysis for the investigation of Wilson’s disease using μ XRF and XANES,” *Metallomics* **8**, 648–653 (2016).
- ²⁹U. Fittschen *et al.*, “A setup for synchrotron-radiation-induced total reflection X-ray fluorescence and X-ray absorption near-edge structure recently commissioned at BESSY II BAMline,” *J. Synchrotron Radiat.* **23**, 820–824 (2016).
- ³⁰M. Menzel *et al.*, “Shading in TXRF: Calculations and experimental validation using a color X-ray camera,” *J. Anal. At. Spectrom.* **30**, 2184–2193 (2015).
- ³¹A. G. Buzanich, M. Radtke, U. Reinholz, H. Riesemeier, and F. Emmerling, “Time- and spatial-resolved XAFS spectroscopy in a single shot: New analytical possibilities for *in situ* material characterization,” *J. Synchrotron Radiat.* **23**, 769–776 (2016).
- ³²A. Kulow *et al.*, “A new experimental setup for time- and laterally-resolved X-ray absorption fine structure spectroscopy in a ‘single shot,’” *J. Anal. At. Spectrom.* **34**, 239–246 (2019).
- ³³C. T. Cakir *et al.*, “Exploring the depths of corrosion: A novel GE-XANES technique for investigating compositionally complex alloys,” *Anal. Chem.* **95**, 4810 (2023).
- ³⁴I. C. B. Martins *et al.*, “Formation mechanism of a nano-ring of bismuth cations and mono-lacunary Keggin-type phosphomolybdate,” *Chem. Eur. J.* **28**, e202200079 (2022).
- ³⁵A. G. Buzanich *et al.*, “Observation of early ZIF-8 crystallization stages with X-ray absorption spectroscopy,” *Soft Matter* **17**, 331–334 (2021).
- ³⁶J. Andersen and J. Mack, “Mechanochemistry and organic synthesis: From mystical to practical,” *Green Chem.* **20**, 1435–1443 (2018).
- ³⁷A. A. Michalchuk, A. Kabelitz, and F. Emmerling, “Monitoring mechanochemical processes *in situ* and in real time,” in *Nontraditional Activation Methods in Green and Sustainable Applications* (Elsevier, 2021), pp. 369–419.
- ³⁸F. Gomollón-Bel, “Ten chemical innovations that will change our world: IUPAC identifies emerging technologies in chemistry with potential to make our planet more sustainable,” *Chem. Int.* **41**, 12–17 (2019).
- ³⁹A. A. L. Michalchuk and F. Emmerling, “Time-resolved *in situ* monitoring of mechanochemical reactions,” *Angew. Chem., Int. Ed.* **61**, e202117270 (2022).
- ⁴⁰J. Li, Q. Fang, and P. K. Liaw, “Microstructures and properties of high-entropy materials: Modeling, simulation, and experiments,” *Adv. Eng. Mater.* **23**, 2001044 (2021).
- ⁴¹M.-H. Tsai and J.-W. Yeh, “High-entropy alloys: A critical review,” *Mater. Res. Lett.* **2**, 107–123 (2014).
- ⁴²J. Baumann, Y. Kayser, and B. Kanngießner, “Grazing emission X-ray fluorescence: Novel concepts and applications for nano-analytics,” *Phys. Status Solidi B* **258**, 2000471 (2021).
- ⁴³F. Meirer, G. Pepponi, C. Strelti, P. Wobruschek, and N. Zoeger, “Grazing exit versus grazing incidence geometry for x-ray absorption near edge structure analysis of arsenic traces,” *J. Appl. Phys.* **105**, 074906 (2009).
- ⁴⁴O. Scharf *et al.*, “Compact pnCCD-based X-ray camera with high spatial and energy resolution: A color X-ray camera,” *Anal. Chem.* **83**, 2532–2538 (2011).
- ⁴⁵M. F. Guerra and T. Calligaro, “Gold traces to trace gold,” *J. Archaeol. Sci.* **31**, 1199–1208 (2004).
- ⁴⁶M. F. Guerra, M. Radtke, I. Reiche, H. Riesemeier, and E. Strub, “Analysis of trace elements in gold alloys by SR-XRF at high energy at the BAMline,” *Nucl. Instrum. Methods Phys. Res., Sect. B* **266**, 2334–2338 (2008).
- ⁴⁷M. F. Guerra, T. Calligaro, M. Radtke, I. Reiche, and H. Riesemeier, “Fingerprinting ancient gold by measuring Pt with spatially resolved high energy Sy-XRF,” *Nucl. Instrum. Methods Phys. Res., Sect. B* **240**, 505–511 (2005).
- ⁴⁸I. Reiche *et al.*, “Discovering vanished paints and naturally formed gold nanoparticles on 2800 years old Phoenician ivories using SR-FF-microXRF with the Color X-ray Camera,” *Anal. Chem.* **85**, 5857–5866 (2013).
- ⁴⁹L. J. R. Higgins, C. J. Sahle, M. Balasubramanian, and B. Mishra, “X-ray Raman scattering for bulk chemical and structural insight into green carbon,” *Phys. Chem. Chem. Phys.* **22**, 18435–18446 (2020).
- ⁵⁰S. R. Gottesman and E. E. Fenimore, “New family of binary arrays for coded aperture imaging,” *Appl. Opt.* **28**, 4344 (1989).
- ⁵¹J. Buchriegler *et al.*, “Enhancements in full-field PIXE imaging—Large area elemental mapping with increased lateral resolution devoid of optics artefacts,” *X-Ray Spectrom.* **47**, 327–338 (2018).
- ⁵²S. Karafiludis *et al.*, “Template-free synthesis of mesoporous and amorphous transition metal phosphate materials,” *Nanoscale* **15**, 3952–3966 (2023).
- ⁵³B. Cantor, I. T. H. Chang, P. Knight, and A. J. B. Vincent, “Microstructural development in equiatomic multicomponent alloys,” *Mater. Sci. Eng. A* **375–377**, 213–218 (2004).
- ⁵⁴J.-W. Yeh *et al.*, “Nanostructured high-entropy alloys with multiple principal elements: Novel alloy design concepts and outcomes,” *Adv. Eng. Mater.* **6**, 299–303 (2004).
- ⁵⁵D. B. Miracle and O. N. Senkov, “A critical review of high entropy alloys and related concepts,” *Acta Mater.* **122**, 448–511 (2017).
- ⁵⁶A. Sarkar *et al.*, “High-entropy oxides: Fundamental aspects and electrochemical properties,” *Adv. Mater.* **31**, 1806236 (2019).
- ⁵⁷S. H. Albedwawi, A. AlJaberi, G. N. Haidemenopoulos, and K. Polychronopoulou, “High entropy oxides—exploring a paradigm of promising catalysts: A review,” *Mater. Des.* **202**, 109534 (2021).
- ⁵⁸A. Smekhova *et al.*, “Inner relaxations in equiatomic single-phase high-entropy cantor alloy,” *J. Alloys Compd.* **920**, 165999 (2022).
- ⁵⁹A. Smekhova *et al.*, “Local structure and magnetic properties of a nanocrystalline Mn-rich Cantor alloy thin film down to the atomic scale,” *Nano Res.* **16**, 5626 (2023).
- ⁶⁰A. Smekhova *et al.*, “Al-driven peculiarities of local coordination and magnetic properties in single-phase Al_x-CrFeCoNi high-entropy alloys,” *Nano Res.* **15**, 4845 (2022).
- ⁶¹J. Timoshenko, A. Kuzmin, and J. Purans, “EXAFS study of hydrogen intercalation into ReO₃ using the evolutionary algorithm,” *J. Phys.: Condens. Matter* **26**, 055401 (2014).
- ⁶²J. Timoshenko, A. Kuzmin, and J. Purans, “Reverse Monte Carlo modeling of thermal disorder in crystalline materials from EXAFS spectra,” *Comput. Phys. Commun.* **183**, 1245–1245 (2012).
- ⁶³D. Menga, A. Guilherme Buzanich, F. Wagner, and T. Feller, “Evaluation of the specific activity of M–N–Cs and the intrinsic activity of tetrapyrrolic FeN₄ sites for the oxygen reduction reaction,” *Angew. Chem., Int. Ed.* **61**, e202207089 (2022).
- ⁶⁴L. C. Pardo Pérez *et al.*, “Determining structure-activity relationships in oxide derived Cu–Sn catalysts during CO₂ electroreduction using X-ray spectroscopy,” *Adv. Energy Mater.* **12**, 2103328 (2022).
- ⁶⁵A. Dubey *et al.*, “Mono-, di-, and tri-valent cation doped BiFe_{0.95}Mn_{0.05}O₃ nanoparticles: Ferroelectric photocatalysts,” *Adv. Funct. Mater.* **32**, 2207105 (2022).
- ⁶⁶C. Brieger *et al.*, “A combined *in-situ* XAS–DRIFTS study unraveling adsorbate induced changes on the Pt nanoparticle structure,” *J. Catal.* **339**, 57–67 (2016).
- ⁶⁷C. Lutz *et al.*, “Evidence for redox reactions during vanadium crossover inside the nanoscopic water-body of Nafion 117 using X-ray absorption near edge structure spectroscopy,” *J. Power Sources* **483**, 229176 (2021).

- ⁶⁸B. Kunkel, A. Kabelitz, A. Guilherme Buzanich, and S. Wohlrab, “Increasing the efficiency of optimized V-SBA-15 catalysts in the selective oxidation of methane to formaldehyde by artificial neural network modelling,” *Catalysts* **10**, 1411 (2020).
- ⁶⁹O. San, “The digital twin revolution,” *Nat. Comput. Sci.* **1**, 307–308 (2021).
- ⁷⁰K. Klementiev and R. Chernikov, “Powerful scriptable ray tracing package xrt,” *Proc. SPIE* **9209**, 92090A (2014).
- ⁷¹M. Noack, gpCAM v6, 2021.
- ⁷²B. Shahriari, K. Swersky, Z. Wang, R. P. Adams, and N. de Freitas, “Taking the human out of the loop: A review of Bayesian optimization,” *Proc. IEEE* **104**, 148–175 (2016).
- ⁷³M. Lifshits, *Lectures on Gaussian Processes* (Springer Berlin Heidelberg, 2012).
- ⁷⁴M. A. Ziatdinov *et al.*, “Hypothesis learning in automated experiment: Application to combinatorial materials libraries,” *Adv. Mater.* **34**, 2201345 (2022).
- ⁷⁵A. Rakotondrajao and M. Radtke, “Machine learning based quantification of synchrotron radiation-induced x-ray fluorescence measurements—A case study,” *Mach. Learn.: Sci. Technol.* **2**, 025004 (2020).
- ⁷⁶E. Kornemann *et al.*, “Miniaturized compound refractive X-ray zoom lens,” *Opt. Express* **25**, 22455 (2017).